

# CMS Draft Analysis Note

*The content of this note is intended for CMS internal use and distribution only*

2018/09/06

Head Id: 469279

Archive Id: 474107:474119M

Archive Date:

Archive Tag: trunk

## Combination of Diboson searches with 2016 data

Thea Klæboe Aarrestad<sup>36</sup>, G. Abbiendi<sup>4</sup>, A. Albert<sup>2</sup>, J. Alcaraz Maestre<sup>22</sup>, A. Alfonsi<sup>13</sup>, Michail Bachtis<sup>7</sup>, Lisa Benato<sup>14</sup>, F. Bispinck<sup>28</sup>, D. Bourilkov<sup>12</sup>, Vieri Candelise<sup>31</sup>, Yu-Hsiang Chang<sup>31</sup>, Ching-Wei Chen<sup>31</sup>, Tongguang Cheng<sup>27</sup>, S.S. Chhibra<sup>4</sup>, Alice Cocoros<sup>16</sup>, R. Cousins<sup>7</sup>, Jordan Damgov<sup>34</sup>, N. De Filippis<sup>3</sup>, B. de la Cruz Martínez<sup>22</sup>, Matteo Defranchis<sup>23</sup>, Phil Duderø<sup>34</sup>, S. Elgammal<sup>6</sup>, F. Errico<sup>3</sup>, A. Escalante del Valle<sup>22</sup>, J. Fernández de Trocóniz<sup>21</sup>, A. Florent<sup>7</sup>, S. Folgueras<sup>27</sup>, Camilla Galloni<sup>36</sup>, Leonardo Giannini<sup>20</sup>, O. González López<sup>22</sup>, Maxime Gouzevitch<sup>19</sup>, Pietro Govoni<sup>23</sup>, Ulrich Heintz<sup>5</sup>, Andreas Hinzmann<sup>14</sup>, Bob Hirosky<sup>35</sup>, K. Hoepfner<sup>28</sup>, Huang Huang<sup>26</sup>, Raman Khurana<sup>31</sup>, Ben Kilminster<sup>36</sup>, D.H. Kim<sup>32</sup>, Michael Krohn<sup>8</sup>, Clemens Lange<sup>1</sup>, A. Lanyov<sup>10</sup>, J.E. Lee<sup>32</sup>, Sung-Won Lee<sup>34</sup>, K.P. Lee<sup>33</sup>, Qiang Li<sup>26</sup>, Hengne Li<sup>35</sup>, Shu-Xiao Liu<sup>31</sup>, Paul Lujan<sup>25</sup>, Devdatta Majumder<sup>18</sup>, Petar Maksimovic<sup>16</sup>, M. Materok<sup>28</sup>, D. Moran<sup>21</sup>, Matthias Mozer<sup>17</sup>, K.W. Nam<sup>33</sup>, N. Neumeister<sup>27</sup>, Jennifer Ngadiuba<sup>1</sup>, Y.D. Oh<sup>32</sup>, M.S. Oh<sup>33</sup>, Marc Osherson<sup>29</sup>, K. Padeken<sup>28</sup>, Neeti Parashar<sup>27</sup>, Jacopo Pazzini<sup>25</sup>, Maurizio Pierini<sup>1</sup>, F. Primavera<sup>13</sup>, B. Radburn-Smith<sup>33</sup>, R. Radogna<sup>3</sup>, Salvatore Rappoccio<sup>24</sup>, Simon Regnard<sup>7</sup>, Andrea Rizzi<sup>20</sup>, Roberto Rossin<sup>25</sup>, Daniela Schäfer<sup>17</sup>, C. Schnaible<sup>7</sup>, J.-F. Schulte<sup>27</sup>, Aniello Spiezia<sup>15</sup>, G. Tansella<sup>3</sup>, Thiago Tomei<sup>30</sup>, Caterina Vernieri<sup>11</sup>, Qun Wang<sup>26</sup>, Yanchu Wang<sup>35</sup>, S. Wiedenbeck<sup>28</sup>, Zijun Xu<sup>26</sup>, Y.C. Yang<sup>32</sup>, H.D. Yoo<sup>33</sup>, Shin-Shan Eiko Yu<sup>31</sup>, Marco Zanetti<sup>25</sup>, and Alberto Zucchetta<sup>36</sup>

<sup>1</sup> CERN

<sup>2</sup> RWTH Aachen University

<sup>3</sup> INFN and Università di Bari

<sup>4</sup> INFN and Università di Bologna

<sup>5</sup> Brown University

<sup>6</sup> CTP, British University

<sup>7</sup> University of California

<sup>8</sup> Colorado University

<sup>9</sup> Cornell University

<sup>10</sup> Joint Institute for Nuclear Research, Dubna

<sup>11</sup> Fermilab

<sup>12</sup> University of Florida

<sup>13</sup> INFN Sezione di Frascati

<sup>14</sup> University of Hamburg

<sup>15</sup> IHEP/CAS Beijing

<sup>16</sup> John Hopkins University

<sup>17</sup> KIT Karlsruhe

<sup>18</sup> Kansas University

- <sup>19</sup> CNRS Lyon  
<sup>20</sup> INFN and Univeristà di Pisa  
<sup>21</sup> CIEMAT and Universidad Autónoma de Madrid  
<sup>22</sup> CIEMAT, Madrid  
<sup>23</sup> INFN and Università di Milano Bicocca  
<sup>24</sup> State University of New York at Buffalo  
<sup>25</sup> Università e INFN sezione di Padova  
<sup>26</sup> Peking University  
<sup>27</sup> Purdue University Northwest  
<sup>28</sup> RWTH Aachen University, III. Phys. Inst. A  
<sup>29</sup> Rutgers University  
<sup>30</sup> SPRACE-UNESP São Paulo  
<sup>31</sup> Taiwan National Central University  
<sup>32</sup> Kyungpook National University  
<sup>33</sup> Seoul National University  
<sup>34</sup> Texas Tech University  
<sup>35</sup> University of Virginia  
<sup>36</sup> University of Zurich

## Abstract

This Analysis Note describes the statistical combination of the searches for heavy resonances decaying to diboson pairs, a lepton and a neutrino, or two leptons. These searches are based on  $35.9 \text{ fb}^{-1}$  of data at  $\sqrt{s} = 13 \text{ TeV}$  collected during the 2016 data taking period. The results are expressed as upper limits on the cross sections of narrow resonances decaying to  $WW$ ,  $WZ$ ,  $ZZ$ ,  $WH$ ,  $ZH$ , and  $HH$ , and as an exclusion on beyond the standard model theories that predict a triplet of heavy vector resonances, and Bulk Graviton models that include the decay into vector bosons.

This box is only visible in draft mode. Please make sure the values below make sense.

PDFAuthor: A. Zucchetta, J.Pazzini, C. Lange  
 PDFTitle: Combination of Diboson searches with 2016 data  
 PDFSubject: CMS  
 PDFKeywords: CMS, physics, diboson

Please also verify that the abstract does not use any user defined symbols

# Contents

1	1	Introduction . . . . .	3
2	2	Theoretical motivations . . . . .	3
3	2.1	Spin-1 resonances . . . . .	4
4	2.2	Spin-2 resonances . . . . .	5
5	3	Event reconstruction . . . . .	7
6	3.1	Electrons . . . . .	7
7	3.2	Muons . . . . .	7
8	3.3	Taus . . . . .	8
9	3.4	Jets . . . . .	8
10	3.5	Jet mass . . . . .	8
11	3.6	N-subjettiness . . . . .	10
12	3.7	Heavy flavor tagging . . . . .	10
13	4	Analyses overview . . . . .	12
14	4.1	All-hadronic final states . . . . .	12
15	4.2	Semi-leptonic final states . . . . .	13
16	4.3	Fully-leptonic final states . . . . .	13
17	4.4	$W'$ analysis . . . . .	14
18	4.5	$Z'$ analysis . . . . .	14
19	4.6	Orthogonality among different channels . . . . .	16
20	5	Statistical combination . . . . .	18
21	5.1	Background systematic uncertainties . . . . .	18
22	5.2	Signal systematic uncertainties . . . . .	19
23	5.3	Correlation among systematic uncertainties . . . . .	20
24	5.4	Signal cross-contamination in the HVT . . . . .	22
25	6	Fit diagnostics . . . . .	24
26	6.1	Fit pulls . . . . .	24
27	6.2	Impacts . . . . .	26
28	6.3	Likelihood scans . . . . .	28
29	6.4	Asymptotic approximation . . . . .	28
30	7	Results . . . . .	30
31	7.1	Model-independent diboson resonances . . . . .	30
32	7.2	$W'$ singlet hypothesis . . . . .	32
33	7.3	$Z'$ singlet hypothesis . . . . .	34
34	7.4	$V'$ triplet hypothesis (HVT) . . . . .	36
35	7.5	Bulk Graviton . . . . .	38
36	8	Summary . . . . .	39
37			

## General information

### Analysis Note v5

Changes with respect to v4:

- Added EXO analyses  $W' \rightarrow \ell \nu$  and  $Z' \rightarrow \ell \ell$
- Performed test with Full CLs

### Analysis Note v4

Changes with respect to v3:

- Major renovation of the AN: introduced “Reconstruction” and “Analyses” sections
- Added missing uncertainties to the datacards
- Added Likelihood scans
- Implemented sharp variations in limits

### Analysis Note v3

Changes with respect to v2:

- Added full authorlist
- Updated B2G-17-006 datacards

### Analysis Note v2

First complete version of the AN. Notes:

- The VW is used in the combination for model-independent limits and the Bulk Graviton interpretation, but not for the HVT, as it is not yet orthogonal

## 1 Introduction

This analysis represents an update of the previous combination based on 2012 and 2015 CMS data at  $\sqrt{s} = 8$  and 13 TeV [1], and describes the statistical combination of the 2016 diboson searches [2–11], providing the most competitive exclusion limits on beyond-the-SM theories that foresee a triplet of heavy vector resonances (HVT) or a Bulk Graviton. In addition, in models where the heavy vector bosons couple predominantly to fermions, the  $W' \rightarrow \ell\nu$  and  $Z' \rightarrow \ell\ell$  decay channels are also considered in the combination [12, 13]. All the considered analyses are based on  $35.9 \text{ fb}^{-1}$  of data at  $\sqrt{s} = 13 \text{ TeV}$  collected during the 2016 data taking period. The mass of the new resonance(s) are expected to exceed 1 TeV, and the SM bosons originating from its decay should have a large Lorentz boost. The SM bosons decays products are thus very collimated, requiring dedicated reconstruction techniques for their identification and reconstruction. In case of hadronic decays, the pair of quarks are reconstructed using a single large-cone jet containing both the two hadronized b quarks.

The analyses cover all possible heavy resonances decays, namely to pair of SM vector bosons (WW, WZ, ZZ), a SM vector boson and a Higgs boson (WH, ZH), a pair of Higgs bosons (HH), or a pair of fermions ( $\ell\ell$  and  $\ell\nu$ ). The different decays of the SM bosons yield a large variety of final states: all-hadronic final states are the result of both bosons decaying to light or heavy quarks offer the most advantageous branching fraction, but are also contaminated by a large QCD multijet background. On the other hand, full-leptonic final states have a very clean signature, but the small branching fractions make these channels not very competitive. A good compromise is represented by mixed decays, where one boson decays leptonically, and the other hadronically. In these cases, the electroweak backgrounds are moderate and well-described by simulation, and the total branching fraction is still significant. A summary of the final states is reported in Table 1.

Table 1: Summary of the diboson analyses based on 2016 data.

	$V \rightarrow q\bar{q}$	$W \rightarrow \ell\nu$	$Z \rightarrow \ell\ell$	$Z \rightarrow \nu\nu$	$H \rightarrow b\bar{b}$	$H \rightarrow \tau\tau$
$V \rightarrow q\bar{q}$	B2G-17-001 [5]	B2G-16-029 [4]	B2G-17-013 [10]	B2G-17-005 [8]	B2G-17-002 [6]	B2G-17-006 [9]
$W \rightarrow \ell\nu$	B2G-16-029 [4]				B2G-17-004 [7]	
$Z \rightarrow \ell\ell$	B2G-17-013 [10]			B2G-16-023 [2]	B2G-17-004 [7]	
$Z \rightarrow \nu\nu$	B2G-17-005 [8]		B2G-16-023 [2]		B2G-17-004 [7]	
$H \rightarrow b\bar{b}$	B2G-17-002 [6]	B2G-17-004 [7]	B2G-17-004 [7]	B2G-17-004 [7]	B2G-16-026 B2G-17-019 [3, 11]	B2G-17-006 [9]
$H \rightarrow \tau\tau$	B2G-17-006 [9]				B2G-17-006 [9]	

## 2 Theoretical motivations

The discovery of Higgs boson by the ATLAS and CMS [14–18] represents the keystone of the standard model (SM) of particle physics. However, a mass of Higgs boson near the electroweak (EW) scale [14, 19–21] either indicates an extreme fine tuning in quantum corrections, or the presence of new physics at the scale of few TeV. Several beyond-the-SM models solve these inconsistency by introducing new heavy spin-1 resonances that may couple to the SM bosons and fermions. An alternative explanation of the Higgs boson mass, which also integrates gravitational interactions, can be provided by the presence of a heavy spin-2 bulk graviton, which is included in models with warped extra dimensions. These resonances are expected to have a mass from few hundreds GeV up to few TeV, and decay to SM vector bosons or the SM Higgs boson, thus being accessible to the LHC.

## 2.1 Spin-1 resonances

Heavy Spin-1 resonances are predicted by several extensions of the standard model such as Minimal Walking Technicolor [22–24], Little Higgs [25–27], or composite Higgs models [28–30]. These models can be generalized by a phenomenological Lagrangian describing the production and decay of spin-1 heavy resonances, such as charged  $W'$  and neutral  $Z'$ , in the heavy vector triplet (HVT) [31] hypothesis. The additional Lagrangian term resulting from the introduction of the heavy triplet has the form:

$$\begin{aligned}\mathcal{L}_V = & -\frac{1}{4}D_\mu V_\nu^a D^\mu V^{\nu a} + \frac{m_V^2}{2}V_\mu^a V^{\mu a} \\ & + ig_V c_H V_\mu^a H^\dagger \tau^a \bar{D}^\mu H + \frac{g^2}{g_V} c_F V_\mu^a \sum_f \bar{f}_L \gamma^\mu \tau^a f_L \\ & + \frac{g_V}{2} c_{VVV} \epsilon_{abc} V_\mu^a V_\nu^b D^\mu V^{\nu c} + \text{quadrilinear terms}\end{aligned}$$

The HVT couplings are parametrized in terms of four parameters:

$c_H$  describes interactions of the new resonance involving the Higgs boson or longitudinally polarized SM vector bosons;

$c_F$  describes the direct interactions of the new resonance with fermions;

$g_V$  is the typical strength of the new interaction;

$M_V$  is the mass of the new resonances, which are degenerate in mass.

The  $W'$  and  $Z'$  bosons couple to the fermions through the combination of parameters  $g^2 c_F / g_V$  and to the Higgs and vector bosons through  $g_V c_H$ , where  $g$  is the  $SU(2)_L$  gauge coupling.

The production of  $W'$  and  $Z'$  at hadron colliders is dominated by the process  $q\bar{q}' / q\bar{q} \rightarrow W' / Z'$ .

Two benchmark models are provided in Ref. [31]:

- In model A, weakly coupled vector resonances arise from an extension of the SM gauge group such as the SSM. The parameters are  $g_V = 1$ ,  $c_H = -g^2 / g_V^2$  and  $c_F = 1$ ;
- In model B, the heavy vector triplet is produced in a strongly coupled scenario, for example in a Composite Higgs model. The parameters assumed for this scenario are  $g_V = 3$ ,  $c_H = -1$  and  $c_F = 1$ .

Consequently, in model A, the branching fractions to fermions and gauge bosons are comparable, whereas for model B, fermionic couplings are suppressed, as shown in Fig. 1 and 3. Therefore, in the context of  $WW$ ,  $WZ$ ,  $ZH$ , and  $WH$  resonance searches, the scenario of model B is of higher interest, because sensitivity to the scenario of model A is dominated by searches in final states with fermions, as visible in Fig. 3. The heavy resonances that couple to  $W'$  and  $Z'$  are considered as a SM custodial triplet, where  $W'$  and  $Z'$  are degenerate in mass and the branching fractions  $\mathcal{B}(W' \rightarrow WH)$  and  $\mathcal{B}(Z' \rightarrow ZH)$  are comparable to  $\mathcal{B}(W' \rightarrow WZ)$  and  $\mathcal{B}(Z' \rightarrow WW)$ . In addition, the singlet hypothesis is also considered, although this is not specifically included in the HVT, but it is foreseen in several BSM models such as minimal  $W'$  and  $Z'$ . In this case, the heavy resonances that couple to  $W'$  and  $Z'$  are a SM singlet, and only a charged or a neutral resonance is expected at a given mass, as summarized in Table 2.

Table 2: Summary of the properties of the heavy resonance models considered in the combination. The polarization of the produced W/Z boson in all considered models is mostly longitudinal.

model	particles	spin	charge	main production	main decay
HVT model A, $g_V = 1$	$W'$ singlet	1	$\pm 1$	$q\bar{q}'$	$q\bar{q}'$
HVT model A, $g_V = 1$	$Z'$ singlet	1	0	$q\bar{q}$	$q\bar{q}$
HVT model A, $g_V = 1$	$W'+Z'$ triplet	1	$0, \pm 1$	$q\bar{q}/q\bar{q}'$	$q\bar{q}/q\bar{q}'$
HVT model B, $g_V = 3$	$W'$ singlet	1	$\pm 1$	$q\bar{q}'$	WZ, WH
HVT model B, $g_V = 3$	$Z'$ singlet	1	0	$q\bar{q}$	WW, ZH
HVT model B, $g_V = 3$	$W'+Z'$ triplet	1	$0, \pm 1$	$q\bar{q}/q\bar{q}'$	WW, WZ, WH, ZH
RS bulk scenario, $\tilde{k} = 0.5$	$G_{\text{bulk}}$	2	0	$gg$	WW, ZZ, HH

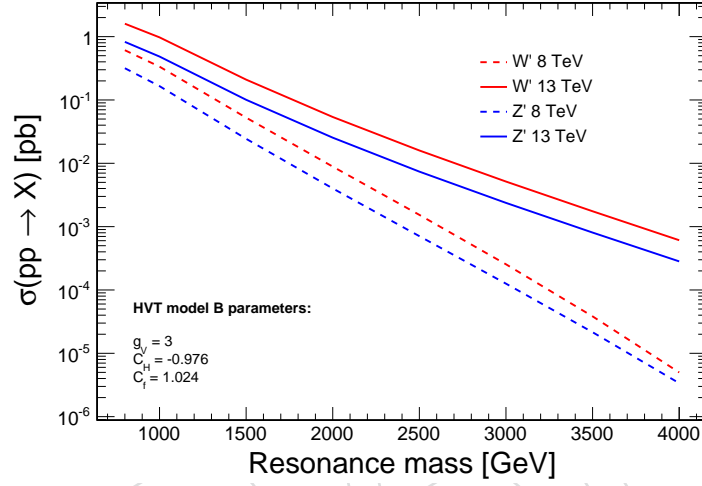


Figure 1: Resonance cross sections as a function of their mass for the HVT benchmark model B [31].

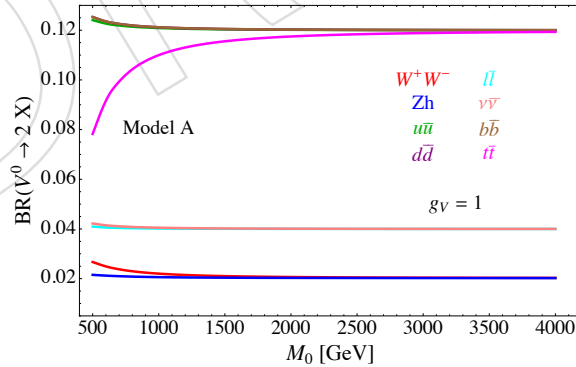


Figure 2: Branching ratios as a function of the resonance mass for the HVT benchmark model A [31].

## 2.2 Spin-2 resonances

Massive resonances of spin-2 can be generically motivated in warped extra dimensional models [32, 33] that predict the existence of a so-called tower of Kaluza–Klein (KK) excitations of a

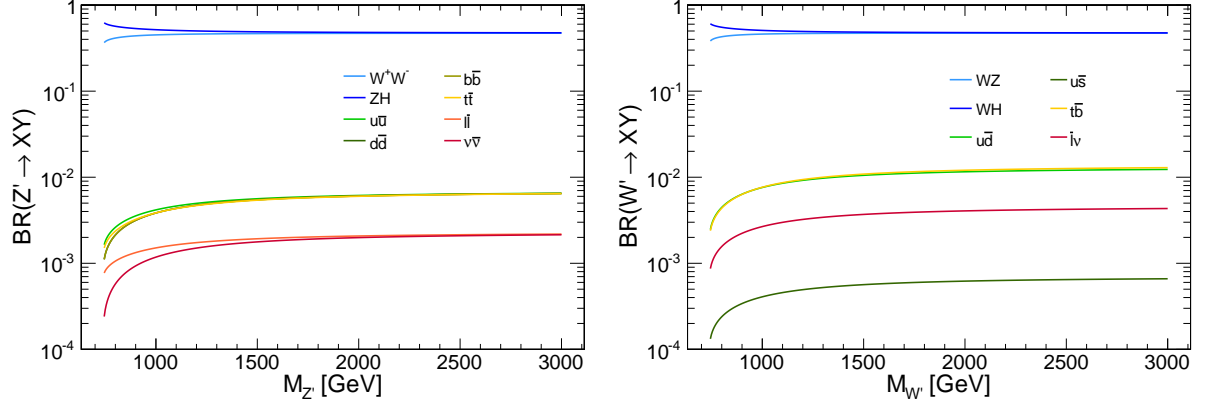


Figure 3: Branching ratios as a function of the resonance mass for a  $Z'$  (left) and  $W'$  (right) in the HVT model B [31].

spin-2 boson, the KK graviton. The original RS model (here denoted as RS1) can be extended to the bulk scenario ( $G_{\text{bulk}}$ ), which addresses in addition the flavor structure of the SM through localization of fermions in the warped extra dimension.

These models have two free parameters: the mass of the first mode of the KK bulk graviton,  $M_G$ , and the ratio  $\tilde{k} \equiv k/\bar{M}_{\text{Pl}}$ , where  $k$  is the unknown curvature scale of the extra dimension, and  $\bar{M}_{\text{Pl}} \equiv M_{\text{Pl}}/\sqrt{8\pi}$  is the reduced Planck mass. The constant  $\tilde{k}$  acts as the coupling constant of the model, on which the production cross-sections and widths of the graviton depend quadratically. For models with  $\tilde{k} \lesssim 0.5$ , the natural width of the resonance is sufficiently small to be neglected when compared to the detector resolution.

In the bulk scenario, coupling of the graviton to light fermions is highly suppressed and the decay into photons is negligible, while in the RS1 scenario branching ratios to photons and fermions are dominant. The production of gravitons at hadron colliders in the bulk scenario is thus dominated by gluon-gluon fusion, while in the RS1 scenario  $q\bar{q}$  and gluon-gluon fusion production contribute equally. The resulting production cross section in the bulk scenario is of order  $10^4$  times lower than in the RS1 scenario. However, in the context of WW and ZZ resonance searches, the bulk scenario is of higher interest, since the RS1 scenario has been strongly constrained in searches with final states with fermions and photons. The two models also differ in the polarization of the produced W and Z bosons. The RS1 graviton decays to transverse polarized bosons 90% of the time, while the bulk graviton decays to longitudinal polarized bosons more than 99% of the time. This leads to differences in the efficiency of the techniques used for identifying the bosons.



### 3 Event reconstruction

The large number of possible decay of the SM bosons result in a broad range of possible final states, involving leptons (electron, muons, and  $\tau$ ) and quarks. The identification of these particles in the detector is usually very similar among the different analyses entering the combination, although some minor differences may arise. In the following sections, the main selections used to identify these candidates are described.

#### 3.1 Electrons

Electron candidates are reconstructed in the fiducial region  $|\eta| < 2.5$  by matching the energy deposits in the ECAL with tracks reconstructed in the tracker [34]. The electron identification is performed by the Particle Flow algorithm, and is based on the distribution of energy deposited along the electron trajectory, the direction and momentum of the track, and its compatibility with the primary vertex of the event.

Further selections are applied by the different analyses depending on the background composition and specific needs (maximum efficiency, or maximum purity). Different set of selections, both approved and validated by the EGamma POG, may be applied. While three analyses base their electron identification on the *cut-based Id*, one other is using the so-called *HEEP Id* selections (Table 3). Both of them include the isolation, defined in a cone of radius 0.3 around the electron direction. Since both algorithms are supported by the POG, a set of scale factors is provided of each algorithm.

Table 3: Summary of the electron selections in the analyses that have electrons in final states.

Analysis	electron Id	working point
B2G-16-023	cut-based	loose
B2G-16-029	HEEP	-
B2G-17-004	cut-based	loose, tight
B2G-17-006	cut-based	
B2G-17-013	cut-based	loose
EXO-16-033	HEEP	-
EXO-16-047	HEEP	-

#### 3.2 Muons

Muons are reconstructed within the acceptance of the CMS muon systems,  $|\eta| < 2.4$ , using the information from both the muon spectrometer and the silicon tracker [35]. Muon candidates are identified via selection criteria based on the compatibility of tracks reconstructed from silicon tracker information only with tracks reconstructed from a combination of the hits in both the tracker and muon detector. Additional requirements are based on the compatibility of the trajectory with the primary vertex, and on the number of hits observed in the tracker and muon systems. Muons are required to be isolated by imposing a limit on the sum of reconstructed tracks within a cone  $\Delta R = 0.4$  around the muon direction, ignoring the muon itself and tracks attributed to other muons [35].

Due to the large average  $p_T$  of the muons, all analyses adopted the *HighPt* muons selections, which has been specifically optimized for muons with  $p_T$  larger than 200 GeV. The isolation of the muon relies on the sum of the  $p_T$  of the tracks within the isolation cone, divided by the muon  $p_T$ ; the ratio should be less than 0.3. However, in channels where a Z is decaying to a pair of muons, the second muon in the event is required to pass a looser selection, in order to avoid losing a significant amount of efficiency if the two muons are close to each other. This

selection, named *TrackerHighPt Id*, is defined using the same quality cuts on the muon track as the *HighPt*, but dropping the requirements that force the muon to be Global or PF:

- to be reconstructed as a standard Tracker muon (was Global muon in *HighPt Id*)
- at least one muon chamber hit included in the global-muon track fit
- muon segments in at least two muon stations
- the track used to obtain the muon momentum needs to pass  $dp_T/p_T < 0.3$ .
- tracker track transverse impact parameter  $d_{xy} < 2\text{mm}$  w.r.t. the primary vertex
- longitudinal impact parameter  $d_z < 5\text{mm}$  w.r.t. the primary vertex
- number of pixel hits  $> 0$
- number of tracker layers with hits  $> 5$ .

The isolation is also based on the tracker isolation, but in case the other muon from the  $Z \rightarrow \mu\mu$  decay falls inside the isolation cone, its contribution is explicitly removed.

The *HighPt* muon selection is approved by the POG, and scale factors are provided to cover the minor identification and isolation discrepancies. The *TrackerHighPt Id* has been blessed by the POG in a later stage, and scale factors are also available.

The muon selections (*HighPt Id* + tracker Iso, and *TrackerHighPt* + tracker Iso in case of two muons) are consistent among all analyses.

### 3.3 Taus

The  $\tau$  leptons are sometimes used as a veto to reduce backgrounds that may yield a large missing energy. However, the  $\tau$  selection is crucial for the B2G-17-006 analysis, which targets the Higgs decays to  $\tau$  leptons and uses a dedicated algorithm [36].

### 3.4 Jets

Jets are used to reconstruct hadronically-decaying W, Z, and Higgs bosons, and play a crucial role in the diboson analyses; the only analysis that does not use jets because is targeting fully leptonic final states is B2G-16-023. The boson candidates are reconstructed from large-cone AK8 jets. Two kind of AK8 jets are used in these searches. The kinematics of the jet are derived from AK8 jets clustered with PF candidates passing the charged hadron subtraction (CHS) algorithm [37], and after the application of the jet energy corrections [38]. The overlap between jets and isolated leptons is removed by removing jets which contain an isolated lepton within their cone size.

The jet substructure variables (mass and N-subjettiness) are instead calculated from AK8 jets built from PUPPI candidates [37, 39], matched to the corresponding CHS jet. The PUPPI algorithm uses a combination of the three-momenta of the particles, event pileup properties, and tracking information in order to compute a weight, assigned to charged and neutral PF candidates, describing the likelihood that each particle originates from a pileup interaction. The weight for charged particles not coming from the primary vertex is 0, and it ranges from 0 to 1 for neutral particles. The weight is used to rescale the particle four-momenta, avoiding the need for further jet-area based pileup corrections.

### 3.5 Jet mass

The jet mass is the key variable that allows the separation between different analyses which share the same final state. The jet mass is calculated from the AK8 PUPPI jets, groomed using

the soft-drop algorithm [40, 41] to remove contributions from soft radiation and additional interactions, with algorithm parameters chosen to be  $\beta = 0$  and  $z_{\text{cut}} = 0.1$ . The jet mass is calculated as the invariant mass of the candidates passing the PUPPI and soft-drop algorithms.

Dedicated mass corrections, derived from simulation and data in a region enriched with  $t\bar{t}$  events with merged  $W(q\bar{q})$  decays, are applied to the jet mass in order to remove residual jet  $p_T$  dependence [6, 42], and to match the jet mass scale and resolution observed in data. The measured soft-drop jet mass resolution is approximately 10%. The jet mass distribution of the signal and the background is shown in Fig. 4.

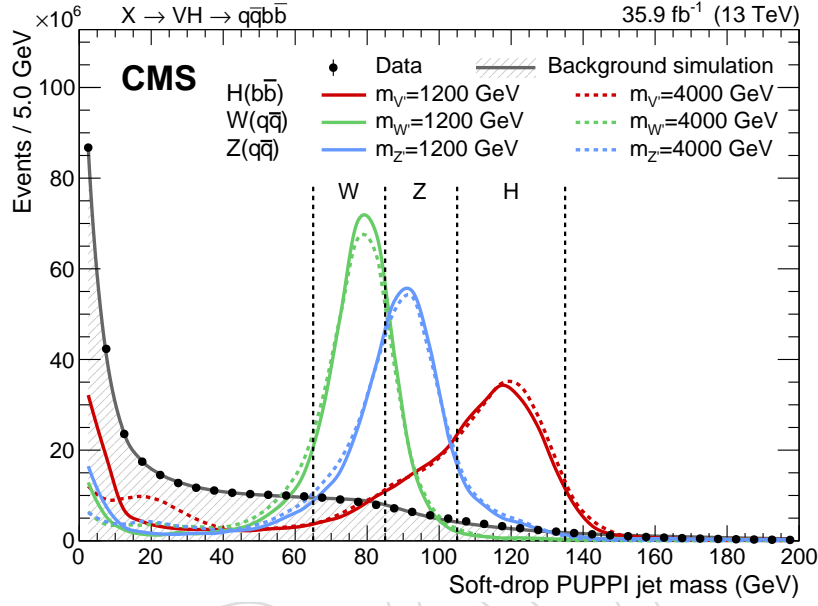


Figure 4: Jet mass for the W, Z, and H bosons compared to the QCD multijet background and data.

The events are divided according to their jet mass value(s). The signal region (SR) is defined as a mass window centered on the nominal mass of the boson:

$$\mathbf{W} \quad 65 < m_j < 85 \text{ GeV}$$

$$\mathbf{Z} \quad 85 < m_j < 105 \text{ GeV}$$

$$\mathbf{H} \quad 105 < m_j < 135 \text{ GeV}$$

Events outside these regions may be used for the background estimation, depending on the analysis strategy. Even though the W and Z mass windows are often used together, analyses never look at both the W/Z and Higgs regions simultaneously. Analyses searching for resonances decaying to hadronic W/Z candidates, even if they do not include events in the H mass window in their SR by construction, they also blind the H region for the background prediction in order to avoid biases from other Higgs signal, and remove the statistical correlation with other analyses. The same is true for the analyses targeting the Higgs, which never use events in the W/Z region. This exclusion is explicitly included in the analyses, as reported in Fig. 5, and guarantees the orthogonality between the different analyses targeting final states with the same number of leptons.

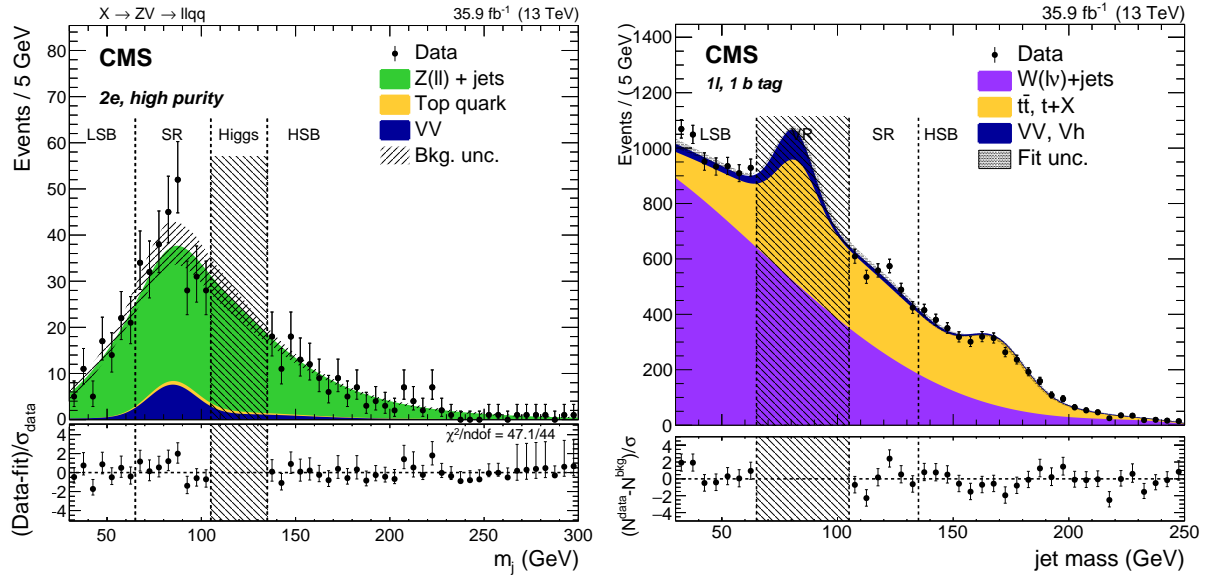


Figure 5: JMass windows in two different analyses, B2G-17-013 (left) and B2G-17-004 (right). The analysis looking for W/Z bosons does not use events in the Higgs mass window, and viceversa.

### 3.6 N-subjettiness

Substructure variables are used to identify single reconstructed jets that result from the merger of more than one parton jet. These variables are calculated on each reconstructed jet before the application of the soft-drop algorithm including the PUPPI algorithm corrections for pileup mitigation. The constituents of the jet are clustered iteratively with the anti- $k_T$  algorithm, and the procedure is stopped when  $N$  subjets are obtained. A variable, the  $N$ -subjettiness [43], is introduced:

$$\tau_N = \frac{1}{d_0} \sum_k p_{T,k} \min(\Delta R_{1,k}, \Delta R_{2,k}, \dots, \Delta R_{N,k}).$$

The index  $k$  runs over the jet constituents and the distances  $\Delta R_{J,k}$  are calculated with respect to the axis of the  $J$ th subjet. The normalization factor  $d_0$  is calculated as  $d_0 = \sum_k p_{T,k} R_0$ , setting  $R_0$  to the radius of the original jet. The variable that best discriminates between quark and gluon jets and jets from two-body decays of massive particles is the ratio of 2-subjettiness and 1-subjettiness,  $\tau_{21} = \tau_2 / \tau_1$ , which lies in the interval from 0 to 1, where small values correspond to a high compatibility with the hypothesis of a massive object decaying into two quarks (Fig. 6). Events are usually divided in two  $\tau_{21}$  intervals to maximize the sensitivity to the signal, although a loose  $\tau_{21}$  selection can still be used in conjunction with other tagging techniques (e.g. b-tagging for a Higgs candidate)

The  $N$ -subjettiness algorithm is the same for all analyses, and consists of the  $\tau_{21}$  calculated after the application of the PUPPI pileup mitigation algorithm. The working points, however, are not the same for all analyses, as reported in Table 4.

### 3.7 Heavy flavor tagging

The b-tagging algorithms are used for multiple purposes: to identify Higgs boson decays to  $b\bar{b}$ , to reject some specific background (usually  $t\bar{t}$ ), or to select control regions. In the two latter cases, it is usually applied to AK4 narrow-cone jets, and the most common tagger employed is the CSVv2. For the Higgs-tagging, there are multiple choices instead. A summary of the

Table 4: Summary of the N-subjettiness selections.

Analysis	n-subjettiness algorithm	working point(s)
B2G-16-026	PUPPI $\tau_{21}$	$\tau_{21} < 0.55$
B2G-16-029	PUPPI $\tau_{21}$	$\tau_{21} < 0.55, 0.55 < \tau_{21} < 0.75$
B2G-17-001	PUPPI $\tau_{21}$	$\tau_{21} < 0.35, 0.35 < \tau_{21} < 0.75$
B2G-17-002	PUPPI $\tau_{21}$	$\tau_{21} < 0.35, 0.35 < \tau_{21} < 0.75$
B2G-17-005	PUPPI $\tau_{21}$	$\tau_{21} < 0.35, 0.35 < \tau_{21} < 0.75$
B2G-17-006	PUPPI $\tau_{21}$	$\tau_{21} < 0.40, 0.40 < \tau_{21} < 0.75$
B2G-17-013	PUPPI $\tau_{21}$	$\tau_{21} < 0.35, 0.35 < \tau_{21} < 0.75$
B2G-17-019	PUPPI $\tau_{21}$	$\tau_{21} < 0.55$

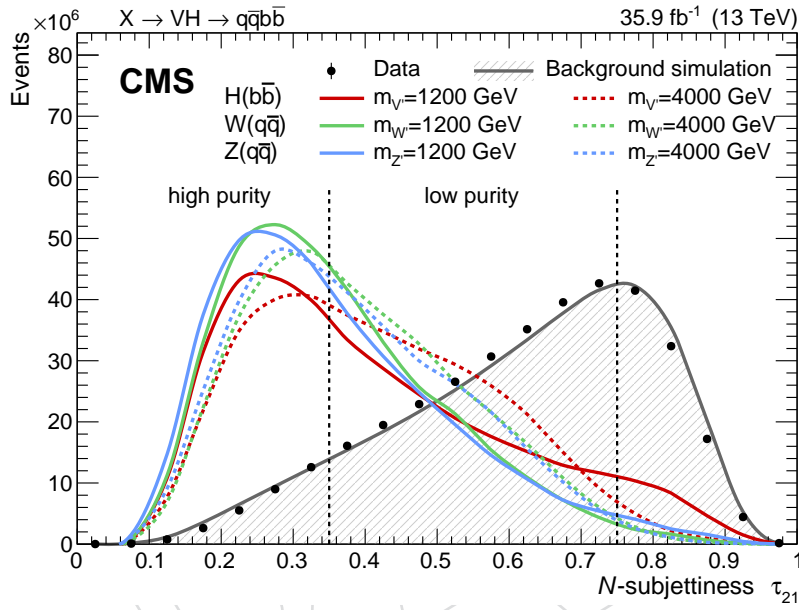


Figure 6: N-subjettiness for different bosons and QCD multijet background.

b-tagging usage is reported in Table 5. The differences are motivated by the final state: in general, the double-b algorithm [44] is more performing against QCD multijet backgrounds. This is the case of the  $X \rightarrow HH \rightarrow 4b$  and  $X \rightarrow VH \rightarrow q\bar{q}b\bar{b}$  analyses, whose background is more than 90% QCD multijets. On the other hand, analyses that have mostly electroweak and  $t\bar{t}$  backgrounds found better performance with the CSVv2 algorithm [45] applied to the Higgs candidate subjects, and splitting events among two categories with 1 or 2 b-tagged subjects.

Table 5: Summary of the b-tagging selections for boosted  $H \rightarrow b\bar{b}$ .

Analysis	b-tagging algorithm	working point
B2G-16-026	double-b	medium tight, loose
B2G-17-002	double-b	tight, loose
B2G-17-004	subjct CSVv2	loose (1 or 2)
B2G-17-006	subjct CSVv2	loose (1 or 2)
B2G-17-019	double-b, DeepCSV	medium tight, medium

## 4 Analyses overview

Searches for resonant diboson production have been performed in a plethora of final states, each one with its peculiarities. Depending on the background composition, different background estimation methods may be used. All the analyses are based on the full 2016 data set, corresponding to an integrated luminosity of  $35.9 \text{ fb}^{-1}$ , collected with the CMS detector at the LHC in pp collisions at a center-of-mass energy of 13 TeV. Due to the much smaller integrated luminosity, searches based on 2015 data have not been considered for the combination. Analogously, 8 TeV searches are not competitive due to the lower center of mass energy which significantly decreases the high mass resonances cross section, and thus are not included.

### 4.1 All-hadronic final states

Searches in all-hadronic final states have been performed targeting VV [5], VH [6], and HH final states [3, 11]. Although these channels retain a significant signal yield, thanks to the large branching fraction of the bosons decaying to hadrons, these analyses have to deal with the overwhelming background represented by the QCD multijet production, which constitute up to 90% of the total background. Subdominant background processes are  $t\bar{t}$  and  $W$  and  $Z$  +jets where the boson decays hadronically.

These analyses select events with hadronic triggers, composed by the logical OR of pure jet and HT triggers, and triggers that also investigate the jet substructure by requiring a certain groomed mass for one jet in the event. Offline, all analyses require the presence of two large-cone AK8 jets with  $p_T > 200 \text{ GeV}$  and an  $\eta$  separation  $|\Delta\eta| < 1.3$  to reject a large fraction of the background. The exception to these selections is represented by B2G-17-019, where one of the two Higgs bosons is reconstructed from two AK4 jets with  $p_T > 30 \text{ GeV}$ .

The background estimation techniques vary depending on the analysis. The B2G-17-001 and B2G-17-002 use the same “dijet-fit” method. Only events entering the SR are used, divided in multiple categories of  $W/Z/H$  jet mass regions, and the high- and low-purity depending on the  $\tau_{21}$  score of the two jets. Higgs candidates are identified through a selection on the double-b tagger discriminator (see Sec. 3.7) instead of the N-subjettiness selection, and are also divided in tight and loose b-tagging categories. Events that do not pass the loose b-tagging working point are discarded. The background is estimated directly from data, assuming that the dijet invariant mass distribution can be described by a smooth, parametrizable, monotonically decreasing function, which is a power law with a number of parameters, including the normalization, between two and five. Starting from the simplest functional form, an iterative procedure based on the Fisher F-test is used to check at 10% CL if additional parameters are needed to model the background distribution. The background function is fitted to the data simultaneously with the signal. Extensive bias tests demonstrate that the choice of the function has a limited impact on the fitted signal strength, compared to the statistical uncertainty.

The B2G-16-026 and B2G-17-019 use two different background prediction methods, depending on the dijet resonant mass. First, the Higgs candidates are identified with the double-b tagger algorithm and a loose selection on the  $\tau_{21}$ . Then, a *anti-tag* region is defined by inverting the b-tagging selection. For dijet masses larger than 1.2 TeV, the data in the tagged and anti-tagged regions is fitted simultaneously with parametric exponential functions, and the signal template. The tag and anti-tag templates are related to each other through a constant parameter, which represents the pass-to-fail ratio ( $R_{p/f}$ ). In the mass region below 1.2 TeV, a second background prediction method (“Alphabet”) is used instead: the  $R_{p/f}$  is measured as a function of the jet mass to account for the small correlations with the tagging algorithm. The  $R_{p/f}$  is then used to rescale, event by event, the dijet mass distribution of the anti-tag region to obtain the



background prediction in the signal region.

## 4.2 Semi-leptonic final states

Searches for VV and VH resonances have been performed in leptonic final states [4, 7–10]. Leptonic final states represent an attractive alternative to hadronic channels, thanks to the large selection efficiency and the natural discrimination offered by high momentum, isolated leptons. Several final states are probed to consider all possible leptonic decay modes of the vector boson: a large amount of missing energy and the absence of isolated leptons is an indication of a  $Z \rightarrow \nu\nu$  decay; a single, isolated lepton and a moderate amount of missing energy can be interpreted as a  $W \rightarrow \ell\nu$  decay; and two opposite sign, same flavor leptons whose invariant mass is compatible with  $m_Z$  are suitable as Z boson candidates. Higgs bosons decaying to  $\tau$ -leptons are identified through special hadronic  $\tau$  reconstruction and dedicated isolation.

The hadronically-decaying vector bosons are identified through the jet mass and a selection on the  $\tau_{21}$ , dividing events in high- and low-purity categories. The Higgs boson is identified through its decay into pair of b-quarks, clustered in the same large-cone jet, with a mass compatible to  $m_H$ . The b tagging identification relies on the splitting of the original jets into two subjets, with either one or both can be independently b tagged.

All analyses, except B2G-16-029, use the same background estimation method, known as “ $\alpha$ -method”. The main background, which is represented by W+jets, Z+jets, or a mixture of the two, is estimated from the jet mass sidebands ( $30 < m_j < 65$  GeV and  $135 < m_j < 250$  GeV) using two steps. First, the normalization is determined by building jet mass templates from simulation of the main backgrounds, and fitting them to the data by leaving the normalization and jet mass shape of the main background unconstrained in the fit. Then, the main background distribution is derived from the VV and VH invariant mass distribution (or transverse mass distribution in case of  $Z \rightarrow \nu\nu$ ) from data in the sidebands, and multiplied by a transfer function from simulation (the  $\alpha$ -function) to extrapolate the shape to the SR. The contribution of the top quark pair production can be as large as 50% in certain channels; its normalization is derived from appropriate control regions, while the SM VV production is still small, and determined from simulation.

The B2G-16-029 analysis introduced a novel signal extraction method based on a 2D fit. The signal and background yields are determined through a maximum likelihood fit, performed in the full  $(m_{WV}, m_j)$  plane, in the full jet mass range ( $30 < m_j < 210$  GeV). The fit is performed using 2D templates for signal and background processes, starting from simulation and introducing shape uncertainties that model the difference between data and simulation in the full search range. The backgrounds are split in two categories: non-resonant background in the jet mass, composed by W+jets, or  $t\bar{t}$  when the jet does not include a W or a top quark, and a resonant background, which is dominated by  $t\bar{t}$  events with merged W and top quark decays. The 2D fit method achieves approximately 20% better results than the background prediction based on the  $\alpha$ -method.

## 4.3 Fully-leptonic final states

Searches for diboson resonances have been performed also in fully leptonic final states [2]. The B2G-16-023 search looks for resonant ZZ production, where one of the Z bosons decays to a pair of electrons or muons, and the other to neutrinos, which escape undetected yielding a large  $E_T^{\text{miss}}$  in the detector. The ZZ final state is included only in Bulk Graviton models, as the  $Z' \rightarrow ZZ$  decay is suppressed. The presence of leptons and neutrinos selects a very clean final state with reduced backgrounds, composed mainly by Z+jets and SM VV production, but the

small branching fraction makes this channel competitive only for small mass values.

The events are collected with leptonic triggers, and the reconstructed  $E_T^{\text{miss}}$  is calibrated using corrections to the hadronic recoil. Only events with  $E_T^{\text{miss}} > 50$  GeV and a Z  $p_T > 100$  GeV are considered. The fit to the data is performed on the transverse mass of the visible Z candidate and the  $E_T^{\text{miss}}$ , where the signal emerges as a broad peak.

#### 4.4 W' analysis

The search for heavy resonances with a single lepton in the final state follows the Sequential Standard Model (SSM) from Ref. [46]. The search for the process  $W' \rightarrow \ell \nu$  uses  $\ell = e, \mu$  and is described by the EXO-16-033 analysis [12].

Interesting events are selected with a single lepton trigger with thresholds of lepton  $p_T > 115(50)$  GeV for electron (muon). In addition, high- $p_T$  electrons may be triggered by a single-photon trigger with a threshold of 175 GeV for the photon  $p_T$ , which is used in a logical "OR" with the single-electron trigger. Offline, electron and muon identification uses reconstruction algorithms optimized for high  $p_T$ . The minimum offline lepton  $p_T$  must be above the lepton trigger threshold. For offline reconstruction, electrons are required to have  $p_T > 130$  GeV and to have  $|\eta| < 1.44$  or  $1.56 < |\eta| < 2.50$ . Muons must have  $p_T > 53$  GeV and  $|\eta| < 2.4$ . Signal events are identified by the presence of an isolated high- $p_T$  lepton. Events with a second lepton with  $p_T > 25$  GeV are rejected. In the electron channel,  $p_T^{\text{miss}}$  is required to be above 150 GeV.

Given the decay in two final state particles, they are expected to be balanced in terms on  $p_T$  and opposite in direction. This kinematics is exploited to suppress background by requiring the ratio of lepton  $p_T$  over missing transverse momentum  $p_T^{\text{miss}}$  to be in the range  $0.4 < p_T/p_T^{\text{miss}} < 1.5$ , and the angular difference between the lepton and  $p_T^{\text{miss}}$ , with  $\Delta\phi(\ell, \vec{p}_T^{\text{miss}}) > 2.5 \approx 0.8\pi$ .

Searching for deviations from the steeply falling  $m_T$  spectrum requires an accurate background estimate at very high transverse masses. For the majority of background sources, the estimate is determined from simulation, based on samples with large event counts at high  $m_T$ . The primary source of background for all signals is the presence of off-peak, high transverse mass tails of the SM  $W \rightarrow \ell \nu$  decays. Other backgrounds arise from multijet events from QCD processes,  $t\bar{t}$  and single top quark production, and from Drell-Yan events. Contributions from dibosons (WW, WZ, ZZ) decaying to e or  $\mu$  are also considered.

For simulated events passing all the selection criteria, the signal efficiency for an SSM  $W'$  with no requirement on the reconstructed  $m_T$  in the event, is maximal at a value of 0.75 (for both decay channels) for a  $W'$  boson mass range 1.5–2.5 TeV, and decreases gradually to  $\approx 0.60$  for larger and smaller masses. For larger masses, the increasing off-shell production displaces events to lower  $m_T$ , where the background is larger.

No significant excess over the SM expectation is observed in the  $m_T$  spectrum. The highest transverse mass events observed have  $m_T \sim 2.6$  and  $m_T \sim 2.9$  TeV in the electron and muon channels, respectively.

#### 4.5 Z' analysis

The  $Z'$  analysis EXO-16-047 [13] is searching for resonances that decay into a pair of very energetic electron or muons. A shape analysis of the dilepton invariant mass spectra is performed for the search for new physics and the results are interpreted in the context of specific BSM models. A crucial aspect of the analysis is an efficient identification of extremely high  $p_T$  leptons.



The electron candidates are also required to pass a set of dedicated high energy electron selection criteria [34]. Only well-measured tracks that are consistent with originating from the same vertex as the electron are included in the isolation sum. The efficiency of the trigger to select events with two electrons passing the analysis selection requirements is 98.5%, when the barrel (endcap) electrons satisfy  $p_T > 36$  (38) GeV. This primary trigger is monitored by a suite of higher-threshold triggers which have progressively fewer selection requirements, culminating in a trigger that simply requires 800 GeV of  $p_T$  in the ECAL. These triggers are included to minimize the chance that unexpected reconstruction problems cause a lower than expected efficiency in the primary trigger. In the selection of dielectron pairs, at least one of the two electrons must be in the ECAL barrel region in order to reduce the background from multijet events. This also allows the endcap-endcap events to be used as a control sample for the QCD background estimate. Dielectron pairs are not required to be oppositely charged as this leads to a significant efficiency loss at high invariant mass. If there are multiple possible dielectron pairs, the pair with the two highest  $p_T$  electrons is selected. The efficiency to trigger, reconstruct, and select an electron pair with invariant mass equal to 1 TeV within the detector acceptance is 69 (65)% for barrel-barrel (barrel-endcap) events. The experimental mass resolution is 1.0 (1.5)% for barrel-barrel (barrel-endcap) electron pairs with a mass of 1 TeV.

A candidate muon pair at the L1 trigger is required to have at least one muon reconstructed with segments in the muon detectors and transverse momentum  $p_T$  above 22 GeV. These muons are then required to have  $p_T > 50$  GeV and  $|\eta| < 2.4$  at the HLT. The trigger efficiency for dimuon events, where both muons have  $p_T > 53$  GeV, is measured to be around 99.5% if both muons are in the barrel ( $|\eta| < 1.2$ ), and 99.0% for events with one muon in the endcap ( $|\eta| > 1.2$ ). High- $p_T$  ( $> 200$  GeV) muon offline reconstruction uses dedicated algorithms [35] to take into account the effects of radiative processes of high-energy muon interactions with the detector material. Muon candidates are also required to pass isolation requirements. The summed  $p_T$  of tracks within a cone of radius  $\Delta R = 0.3$  around the candidate direction should be less than 10% of the  $p_T$  of the candidate, excluding from summation the muon candidate under consideration. Oppositely charged muon candidates passing the selection are combined to form dimuon candidates. The angle between the directions of the two muon candidates is required to be less than  $\pi - 0.02$  in order to suppress cosmic ray backgrounds. If there are multiple possible dimuon pairs, the pair with the two highest  $p_T$  muons is selected. The efficiency to trigger, reconstruct, and select a muon pair with invariant mass equal to 1 TeV within the detector acceptance is  $92.7^{+0.3}_{-0.5}\%$  ( $92.5^{+0.7}_{-2.7}\%$ ) for barrel-barrel (barrel-endcap and endcap-endcap) events. The efficiency for each of the two muons is correlated as is the case for electron pairs. The resolution for muon pairs with a mass of 1 TeV is  $3.0 \pm 0.5$  ( $4.0 \pm 0.6$ )% for barrel-barrel (barrel-endcap and endcap-endcap) events.

The signal cross section corresponds to that obtained in the narrow width approximation; specifically, off-shell contributions from PDFs and interference effects are not included. The signal probability density function (pdf) used is a convolution of a Breit-Wigner (BW) function and a Gaussian function with exponential tails to either side (Cruijff). The BW function models the intrinsic width of the particle, while the Cruijff function models the detector response. A Crystal Ball (CB) function better describes the signal shape at higher dielectron masses compared to the Cruijff function. Therefore for  $m_{ee} > 2300$  GeV, a CB function is used.

The dominant SM background arises from the DY process. Other sources of background are real leptons from the top quark-antiquark ( $t\bar{t}$ ), single top quark ( $tW$ ), diboson ( $WW$ ,  $WZ$ , and  $ZZ$ ), and DY  $\tau^+\tau^-$  processes. The background pdf for the dielectron channel is parametrized

by the following formula:

$$\begin{aligned} m^\kappa \exp\left(\sum_{i=0}^3 \alpha_i m^i\right), & \quad \text{if } m \leq 600 \text{ GeV} \\ m^\lambda \exp\left(\sum_{i=0}^3 \beta_i m^i\right), & \quad \text{if } m > 600 \text{ GeV}, \end{aligned} \quad (1)$$

while for the dimuon channel the following functional form is used:

$$\begin{aligned} m^\mu \exp\left(\sum_{i=0}^2 \gamma_i m^i\right), & \quad \text{if } m \leq 500 \text{ GeV} \\ m^\nu \exp\left(\sum_{i=0}^3 \delta_i m^i\right), & \quad \text{if } m > 500 \text{ GeV}. \end{aligned} \quad (2)$$

For each final state, the parameters of the background pdf are obtained by fitting the total background distribution produced using SM MC generators and the background arising from misidentified jets deduced from the data.

The data is found to be in agreement with standard model expectations. Upper limits at 95% confidence level on the product of a narrow-resonance production cross section and branching fraction to dileptons have been calculated in a model-independent manner to enable interpretation in the framework of models predicting a narrow dielectron or dimuon resonance. A scan of different intrinsic width hypotheses is also performed.

Limits are set on the masses of various hypothetical particles. For the  $Z'_{SSM}$  particle, which arises in the sequential standard model, and for the superstring-inspired  $Z'_\psi$  particle, 95% confidence level lower mass limits for the combined channels are found to be 4.50 TeV and 3.90 TeV, respectively. These limits extend the previous ones from CMS by 1.1 TeV in both models. The corresponding limits for Kaluza–Klein gravitons arising in the Randall–Sundrum model of extra dimensions with coupling parameters  $k/\bar{M}_{\text{Pl}}$  of 0.01, 0.05, and 0.10 are 2.10, 3.65, and 4.25 TeV, respectively. The limits extend previous published CMS results by 0.6 (1.1) TeV for a  $k/\bar{M}_{\text{Pl}}$  value of 0.01 (0.10). Finally, limits at 95% confidence level are obtained for the masses of the dark matter particle and its associated mediator, in a simplified model of dark matter production via a vector or axial vector mediator.

## 4.6 Orthogonality among different channels

All analyses are statistically independent on each other, i.e. they do not share events by construction. Orthogonality is achieved through lepton selections, number of jets, and jet mass windows. Analyses with 0 leptons in the final state explicitly veto the presence of isolated electron, muons, and taus. Analyses with 1 lepton in the final state apply vetoes on additional leptons, thus removing any overlap with 2 lepton final states. All-hadronic analyses apply an upper cut on the  $E_T^{\text{miss}}$  to avoid overlaps with  $0\ell$  searches to 200 or 250 GeV, and veto isolated leptons. Analyses that share the same lepton multiplicity avoid overlaps by selecting different jet mass windows: the W mass window  $m_W$  ( $65 < m_j < 85 \text{ GeV}$ ), the Z mass window  $m_Z$  ( $85 < m_j < 105 \text{ GeV}$ ), and the Higgs mass window  $m_H$  ( $105 < m_j < 135 \text{ GeV}$ ). In some analyses, the W and Z mass windows are considered together, and the resulting region is commonly referred to as the V mass window  $m_V$  ( $65 < m_j < 105 \text{ GeV}$ ). Table 6 summarizes the fundamental selections that achieve complete orthogonality. However, one analysis, B2G-16-029, is currently not orthogonal with the others, due to its background prediction strategy, which

scans the whole jet mass spectrum. Therefore, this analysis is not orthogonal by construction with other channels, and especially the WH channel. For this reason, it is removed from the  $W', Z', V'$  interpretation. In the Bulk Graviton interpretation, the WH channel does not contribute, and thus the B2G-16-029 can be included in the combination. The same is true for the model-independent limits on WW and WZ production.

Table 6: Summary of the basic leptonic and hadronic selections that guarantee the orthogonality between analyses. The symbol  $\ell$  represents electrons and muons;  $\tau$ -leptons are considered separately. The  $E_T^{\text{miss}}$  column indicates a large amount of  $E_T^{\text{miss}}$  ( $> 250$  GeV); individual analyses may apply additional and less stringent requirements on  $E_T^{\text{miss}}$ , but this is not crucial in determining the orthogonality. The exact values of the jet mass windows are reported in the text. The reported b-jets are additional b-tagged AK4 jets, other than (b-tagged) AK8 jet. The X symbol indicates an explicit veto.

Analysis	$\ell$	$\tau$	$E_T^{\text{miss}}$	AK8 jets	AK8 jet mass SR	b-jets	notes
B2G-16-023	2	-	✓	-	-	-	
B2G-16-026	-	-	-	2	$2 \times m_H$	-	
B2G-16-029	1	-	-	1	all $m_j$	X	
B2G-17-001	X	-	-	2	$2 \times [m_W, m_Z]$	-	
B2G-17-002	X	X	X	2	$1 \times [m_W, m_Z], 1 \times m_H$	-	
B2G-17-004	0,1,2	X	✓	1	$1 \times m_H$	X	$\Delta\phi(\ell, p_T^{\text{miss}}) < 2$
B2G-17-005	X	X	✓	1	$1 \times m_V$	X	
B2G-17-006	-	2	✓	1	$1 \times [m_W, m_Z, m_H]$	X	
B2G-17-013	2	-	-	1	$1 \times m_V$	-	$70 < m_{\ell\ell} < 110$ GeV
B2G-17-019	-	-	-	1	$2 \times m_H$	2	
EXO-16-033	1	-	-	-	-	-	$\Delta\phi(\ell, E_T^{\text{miss}}) > 2.5$
EXO-16-047	2	-	-	-	-	-	$m_{\ell\ell} > 120$ GeV

## 5 Statistical combination

The method consists in the classic search for a narrow peak on top of the smoothly falling background spectrum. For each analysis, channel, and signal hypothesis, a likelihood function is built from the reconstructed diboson invariant mass distribution observed in data, the sum of the estimated background processes, and the signal resonance shape, in order to test for the presence of the new resonance. The likelihood function  $\mathcal{L}$ , computed using events binned as a function of reconstructed diboson invariant mass, is

$$\mathcal{L}(\mu; \text{data}) = \prod_i \frac{\lambda_i^{n_i} e^{-\lambda_i}}{n_i!}, \quad (3)$$

where  $\lambda_i = \mu N_i(S) + N_i(B)$ ,  $\mu$  is a scale factor for the signal,  $N_i(S)$  is the number expected from the signal in the  $i^{\text{th}}$  mass bin, and  $N_i(B)$  is the number expected from background. The parameter  $n_i$  is the number of data events in the  $i^{\text{th}}$  mass bin. The likelihood is maximized to obtain the best fit  $\mu$  for each signal and resonance mass hypothesis.

### 5.1 Background systematic uncertainties

The treatment of the background parameters in the maximum likelihood fit depends on the analysis: in the B2G-16-029, B2G-17-001, and B2G-17-002 analyses, the background fit function parameters are left floating in the maximum likelihood fit, such that the background prediction is simultaneously obtained with the signal  $\mu$  for every hypothesis. On the other hand, in the other analyses, the background is estimated using data sidebands and uncertainties related to its parametrized shape are treated as nuisance parameters constrained with Gaussian probability density functions in the maximum likelihood fit. A summary of the background estimation method for the different analyses is reported in Table 7. The analyses that are being combined have orthogonal event selections and do not select common data events. The likelihoods of the all channels are thus combined by constructing a combined likelihood from their product.

Table 7: Reminder of the analyses background prediction methods, focusing on whether the parameters describing the (main) background are free to float (unconstrained) or are fixed from the background prediction methods, with the corresponding associated uncertainty.

Analysis	background prediction	unconstrained parameters?
B2G-16-023	MC-based templates	no
B2G-16-026	Alphabet/ Assisted bump-hunt	partially: SR fitted with anti-tag region
B2G-16-029	2D fit	partially: large unc., constrain from data
B2G-17-001	1D fit	yes
B2G-17-002	1D fit	yes
B2G-17-004	$\alpha$ -ratio	no
B2G-17-005	$\alpha$ -ratio	no
B2G-17-006	$\alpha$ -ratio	no
B2G-17-013	$\alpha$ -ratio	no
B2G-17-019	Alphabet	no
EXO-16-033	MC-based templates	no
EXO-16-047	MC-based parametrization	no

## 496

497  
498  
499  
500  
501

502  
503  
504  
505  
506  
507

508  
509  
510  
511  
512  
513  
514  
515

Table 8: Summary of the systematic uncertainties considered in each analyses. The uncertainties labeled with  $\checkmark$  have been added during the combination stage.

[illegible]

### 5.3 Correlation among systematic uncertainties

When the likelihoods of multiple analyses channels are combined, the correlation of systematic effects across analysis channels is taken into account by categorizing the uncertainties into fully correlated (associate to same nuisance parameter) and fully uncorrelated (associate to different nuisance parameters). The correlation or non-correlation among the different sources is not defined a-priori, but it has to be evaluated case by case in Table 9. As a general rule, uncertainties that are channel-dependent, such as background estimation parameters and normalizations, are considered as non-correlated because are derived from statistically-independent regions. On the other hand, experimental uncertainties arising from object reconstruction and identification, e.g. muon, jet mass, and JEC, are considered as correlated between the different channels, because they have each a common source.

Table 9: Summary of the main systematic uncertainties, and their correlation/non-correlation among the different channels/analyses.

	Correlation	Notes
fit parameters	X	stat. independent
bkg. normalization	X	stat. independent
jet energy scale	✓	
jet energy resolution	✓	
jet mass scale	✓	anti-corr. between W/Z cat.
jet mass resolution	✓	anti-corr. between W/Z cat.
e, $\mu$ Id, Iso, trigger	✓	corr. between cut-based and HEEP Id
e, $\mu$ scale and res.	✓	except EXO-16-033 (constrain from bkg)
$\tau$ Id, Iso, trigger	✓	
$\tau$ high- $p_T$ extr.	✓	only $\tau\tau$ analysis
MET scale and res.	✓	
hadronic/MET triggers	✓	only if same trigger and dataset
b-tagging	✓	anti-corr. between 1b and 2b cat.
V tagging	✓	anti-corr. between HP and LP cat.
V high- $p_T$ extr.	✓	anti-corr. between HP and LP cat.
Higgs tagging	✓	only VH and HH
pile-up	✓	
luminosity	✓	
PDF acceptance	✓	
QCD scales	✓	<b>not</b> profiled in the fit
PDF scale	✓	<b>not</b> profiled in the fit

**electron identification** the cut-based and HEEP scale factors uncertainties are taken as correlated, as the algorithms share most of the basic electron variables, and the SF are derived using the same technique (the tag-and-probe on  $Z \rightarrow ee$  events), and the data sample used to derive the SF are also statistically correlated.

**b-tagging** the migration effects between different categories within the same analysis are already taken into account in the different analyses. The CSV scale factors uncertainties are taken as correlated among different analyses, for both AK8 subjets and AK4 jets, because the tagging algorithm is the same, even if the working points have been retuned for subjets. The double-b and CSVv2 scale factor uncertainties are taken as correlated as well, since the two algorithms share a large fraction of the input variables [45], so it can be safely assumed that the multivariate outputs will be correlated as well. Furthermore, the scale factors have been derived in a similar data set, con-



sisting of jets containing one muon for the subjects, or two muons for the double-b. The two scale factors set are thus statistically correlated.

**n-subjettiness** the scale factors for all working points have been measured from data in a sample enriched with merged  $W \rightarrow q\bar{q}$  decays from top quarks [42]. Since the method is the same among all working points, and the events used for the measurement are largely correlated, their corresponding uncertainties are assumed to be correlated as well. The scale factors uncertainties between the High Purity and Low Purity categories are instead already taken as anti-correlated by the single analyses.

**jet mass scale and resolution** the effect and the correlation or anti-correlation of jet mass uncertainties for the signal also depends on the signal hypothesis, as different resonances ( $W'$  or  $Z'$ ) yield different bosons in the final states ( $W$  and  $Z$ ), which induce different migration effects across categories. As an example, the migration effects for one analysis are reported in Fig. 10. In general, these migrations across categories are estimated from the single analyses independently. In the combination, the up/down effect is checked to be consistent across all analyses. The migration effects induce a systematic uncertainty on the yields of the signal; the effect on the resonance shape are instead negligible. The correlation/anti-correlation is propagated to the fit to reflect the migration effects.

Table 10: Jet mass scale and resolution migration effects, as evaluated between the jet mass categories in the B2G-17-002 analysis. Same colors indicate positive correlation; opposite colors indicate anti-correlation. The numbers represent the percentage variation of the signal normalization. The migrations depend on the signal hypothesis ( $W'$  or  $Z'$  singlet, or  $V'$  triplet).

uncertainty		$W'$ singlet	$Z'$ singlet	$V'$ triplet
scale	normalization (H region)	+0.3	+0.8	+0.4
		-0.8	-1.1	-0.9
	normalization (V region)	+0.8	+0.4	+0.4
		-0.9	-0.2	-0.5
	migration (W region)	+2.6	+6.1	+3.3
resolution		-2.2	-6.4	-3.1
	migration (Z region)	+13.2	+3.2	+7.2
		-12.5	-3.8	-7.3
	normalization (H region)	+10.5	+9.2	+10.1
		-11.8	-10.2	-11.2
	normalization (V region)	+3.6	+2.0	+3.0
		-2.9	-0.9	-2.2
	migration (W region)	+7.8	+6.5	+8.3
		-7.9	-10.1	-7.6
	migration (Z region)	+12.0	+7.6	+9.5
		-15.3	-7.9	-10.6

### 5.3.1 $W'$ analysis

The EXO-16-033 analysis uses a different background estimation technique with respect to the other analyses included in the combination. In this case, the background templates are derived directly from MC, and the differences with data are covered by the background modeling and reconstruction uncertainties, which also include the uncertainties on the electron and muon reconstruction, identification, and isolation. As a consequence, the data helps to constrain these uncertainties that affect both the background and the signal. Although this method has the advantage to have better performance, because of the constrain on the signal uncertainties, it is also closely related to the selections and the background of the considered channels. In other words, the constrain effect on the signal uncertainties in a certain channel depends on how the MC models the background in that channel. Therefore propagating this constrain to the other analyses and channels of the combination would not be correct. Although in principle they should be correlated, in the EXO-16-033 case the electron and muon reconstruction, identification, isolation, and energy/momentum scale uncertainties are taken as uncorrelated from the other analyses due to their relation to the background estimation method.

## 5.4 Signal cross-contamination in the HVT

The HVT model predicts the simultaneous decay of the heavy resonances into a pair of vector bosons and a vector boson and a Higgs boson, for approximately  $\sim 50\%$  each. The only way to separate VV and VH decays is the hadronic jet mass, but since the W, Z, and H mass peaks cannot be fully resolved due to the limited experimental resolution, there are cross-contamination effects across the different jet mass regions, as visible in Fig. 4.

Three effects may arise:

1. migration between the W and Z mass windows. This effect is significant, due to the large overlap between the two peaks. Due to its importance, it is naturally taken into account by the singular analyses;
2. migration of Z events in the H mass region. This effect is small for two reasons: the Z upper tails are not large (usually less than 5% of the total normalization), and the probability of the dominant  $Z \rightarrow q\bar{q}$  decay to pass the b-tagging selection of the Higgs is very small. Thus, this effect is negligible;
3. the Higgs contamination in the Z and W mass regions. This effect is not negligible, and there is a finite chance to pass the n-subjettiness selections, as the  $H \rightarrow b\bar{b}$  decay is also two-pronged (see Fig. 4).

The migration effect (3) is then considered when normalizing the signals in the HVT model. This effect is evaluated as the fraction of the VH signal that contributes to the VV signal in the w/Z mass windows. This fraction could be used to rescale the signal normalization. However, the signal shapes of the VV and VH signals are not the same, as shown in Fig. 7. On the other hand, re-parametrizing the signal shapes accounting for the sum of the VV and VH signals is not feasible. Since the migration effect is still overall small, the best estimate is represented by rescaling the VV signal of the fraction of VH signal that falls within the resolution of the peak, discarding events in the tails that wouldn't contribute to the signal fit anyway. This is especially true when fitting for a peak representing a narrow resonances, where the events in the lower signal tails do not contribute significantly to the fit. The overall fraction of the VH signal falling within the V mass windows, and its fraction within the resolution of the VV peak, are reported in Table 11.



Table 11: Estimate of the fraction of VH signal entering the V mass regions, divided by each final state and category. Leptonic V decays are considered together, as there is only one source of migration (the opposite-side jet mass). The two rows report the total fraction (tot.), and the fraction calculated with respect to the events falling within the VV peak resolution (res.).

signal $m_j$ region	WH, $W \rightarrow qq$		
	WW	WZ	ZZ
tot.	12.2%	23.6%	4.9%
res.	9.7%	15.2%	3.0%

signal $m_j$ region	ZH, $Z \rightarrow qq$		
	WW	WZ	ZZ
tot.	3.2%	15.6%	27.1%
res.	1.4%	8.9%	17.9%

signal $m_j$ region	VH, $V \rightarrow \nu\nu, \ell\nu, \ell\ell$		
	W	Z	V(W+Z)
tot.	9.8%	30.1%	40.0%
res.	5.4%	17.8%	23.2%

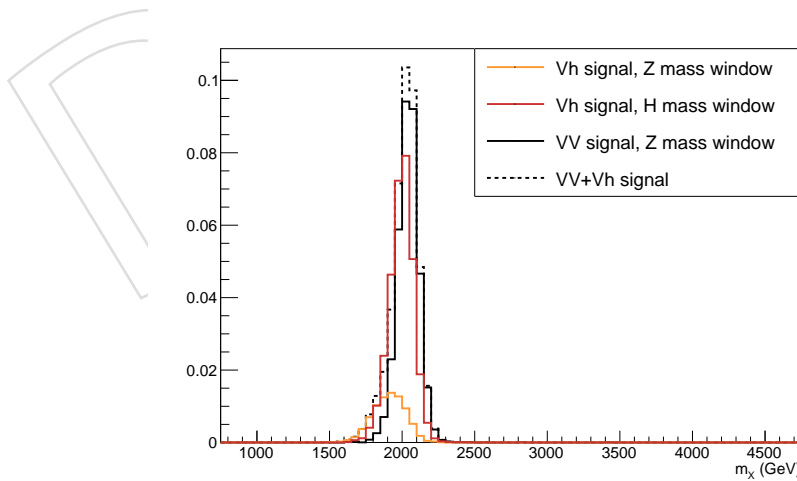


Figure 7: Different signal mass shapes for the  $m_\chi = 2000$  GeV mass points in all-hadronic final states.

## 6 Fit diagnostics

### 6.1 Fit pulls

The signal extraction procedure described above allows the background to vary within the systematics uncertainties modifying the corresponding nuisance parameters. In this section these variations in the background are shown when the fit to the data is performed, both with the background-only and with background plus signal hypothesis.

The bin values represent the pull values  $\Delta x / \sigma_{in}$ , and its error bar the fit constraining on the gaussian width of the nuisance parameter  $\sigma_{out} / \sigma_{in}$ , for both the background-only and the signal+background fit.

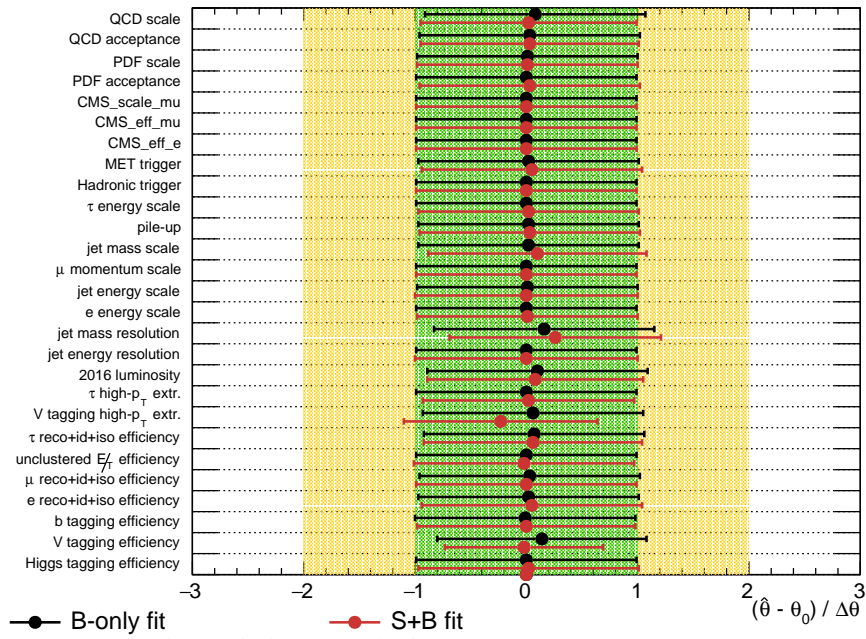


Figure 8: Pull values for the combination of channels contributing to the  $V'$  triplet in both the background-only and signal+background hypotheses. The considered signal mass point is  $m_\chi = 2000 \text{ GeV}$ .

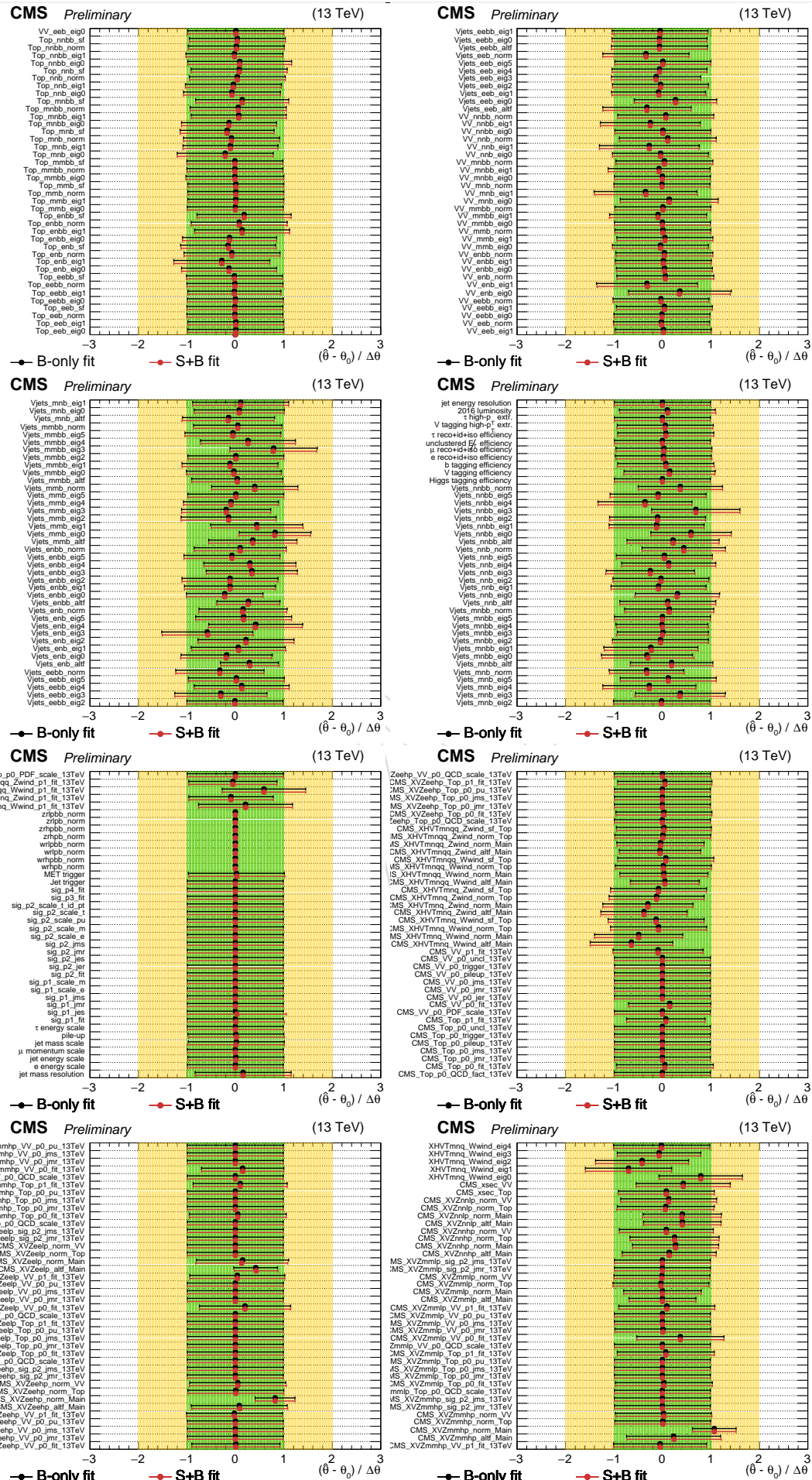


Figure 9: Full list of the pulls for the combination of channels contributing to the  $V'$  triplet and the 3000 GeV mass point.

## 6.2 Impacts

The signal extraction procedure described above allows the background to vary within the systematics uncertainties modifying the corresponding nuisance parameters. The plots report the impacts and the pulls of the fits. The signal normalization uncertainties due to PDF and QCD scales are profiled in the fits.

In the following plots, some uncertainties from free background parameters (used in the B2G-17-001 and B2G-17-002 analyses that employ a fit to data “à la dijet” to estimate the background) show a one-sided impact. For the free background parameters, the impact plots may not be really optimal and/or significant, because each parameter is scanned singularly to derive the impact on the fitted signal strength  $\hat{r}$ , while fixing all the other parameters. This method does not take into account the correlation between parameters, which is especially important with the dijet-fit background prediction method (and less important for the “ $\alpha$ -method”, because uncertainties are already provided as uncorrelated). The side effect is that in the dijet-fit analyses the parameters of the background, other than the considered one, are not allowed to vary, and this may spoil the background estimation which *may* result in a one-sided impact. This effect has been observed in the independent analyses as well to check that it was not introduced in the combination.

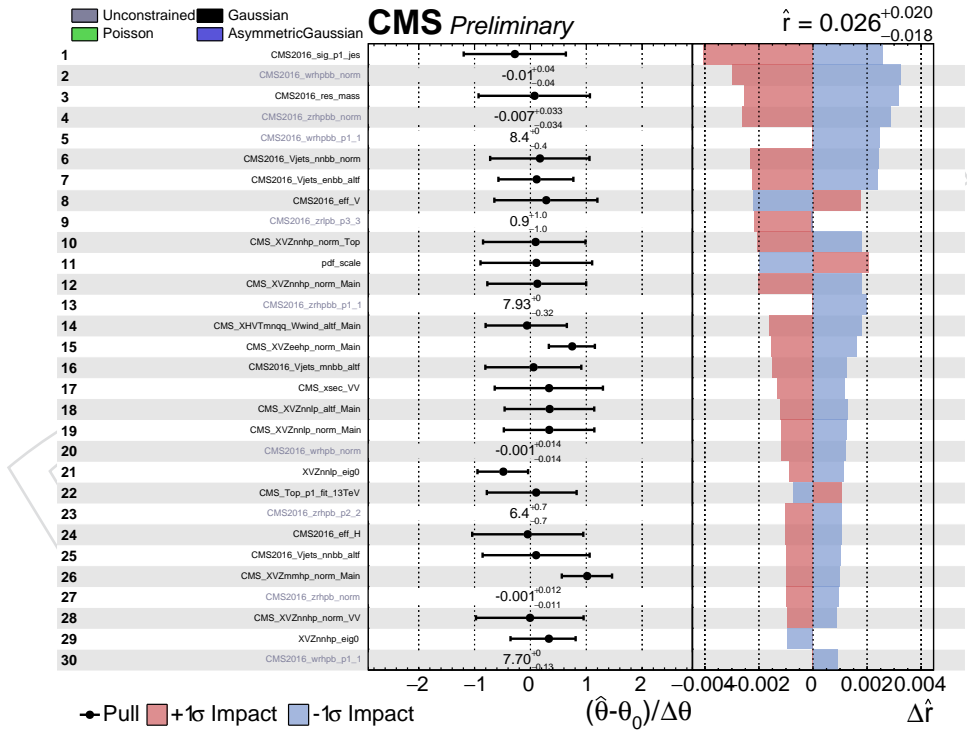


Figure 10: Impacts of the first 30 nuisances for the combination of all channels in the triplet hypothesis with mass 1000 GeV.

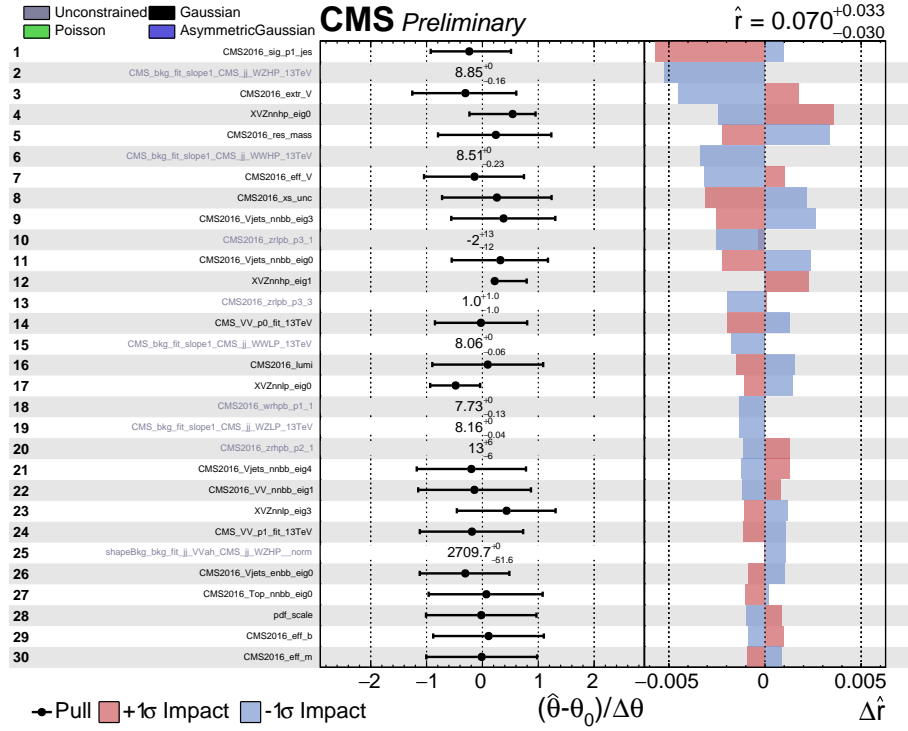


Figure 11: Impacts of the first 30 nuisances for the combination of all channels in the triplet hypothesis with mass 2000 GeV.

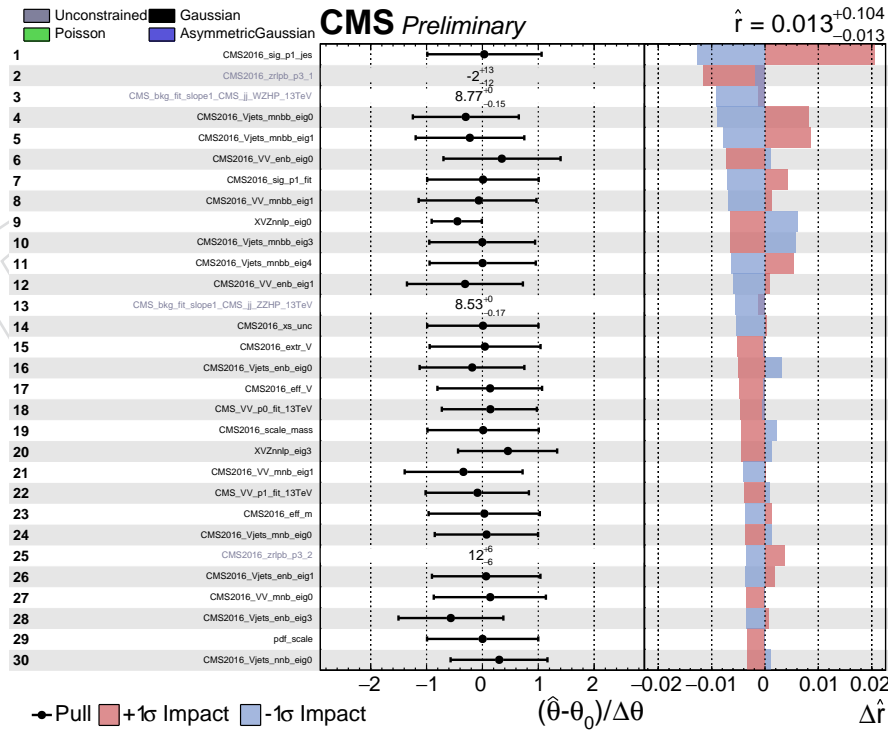


Figure 12: Impacts of the first 30 nuisances for the combination of all channels in the triplet hypothesis with mass 3000 GeV.

### 6.3 Likelihood scans

Likelihood scans are performed to check the value if the Likelihood around the best fir value  $r$ . The scans are performed considering the combination of all analyses contributing to the  $V'$  resonance. Fig. 13 shows the likelihood scans for three sample mass points, corresponding to 1, 2, and 3 TeV, and one mass point for the Graviton combination at 2 TeV. The different profile depends on the observed value: while 1 and 2 TeV have positive best-fit value, the 3 TeV mass point observes only a slight excess, and therefore the  $r$  distribution is asymmetric. Negative  $r$  values are not allowed, as they are not physical.

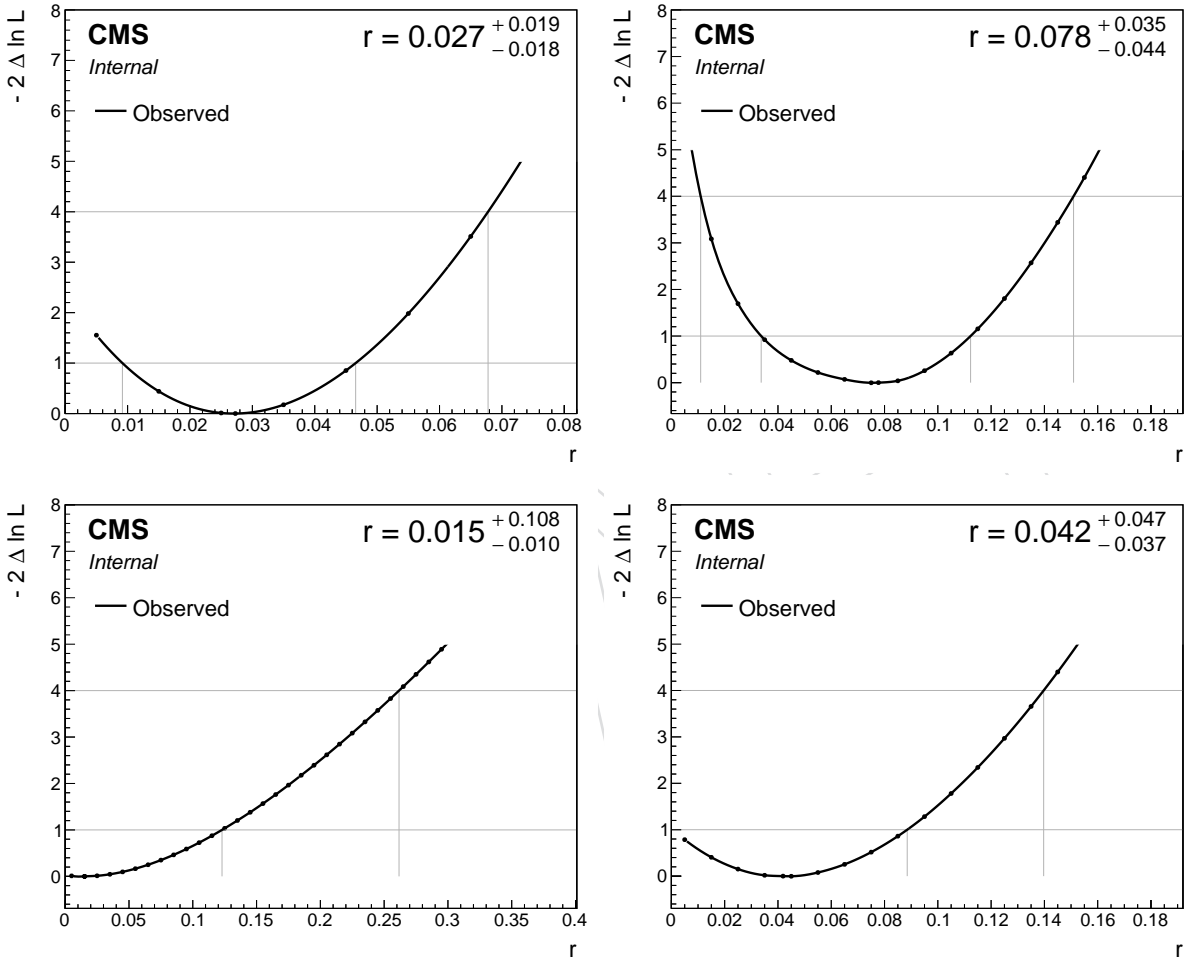


Figure 13: Likelihood scans as a function of the best-fit value  $r$  for different mass points of the  $V'$  combination: 1 TeV (upper left), 2 TeV (upper right), 3 TeV (lower left). One scan for the 2 TeV mass is reported for the Graviton combination (lower right).

### 6.4 Asymptotic approximation

The limits on the new resonances cross sections are derived with the asymptotic modified frequentist method [47]. Although this method is computationally much faster and makes the combination affordable from the CPU-time point of view, it is also known to be inaccurate when the statistics in data is small, as in the tails of the distributions. A cross check has been performed with a high mass point ( $Z' = 4.5$  TeV) by running the non-approximated  $CL_s$  computation and comparing the result with the asymptotic approximation. The observed limit

with the full  $CL_s$  is 11.2, and with the asymptotic approximation 8.7 (arbitrary units). This 28% difference may seem large, but it should be compared to the widths of the 1 and 2 sigma bands, which are distant from the expected limit by a factor 2 each, and thus this difference is tolerable.

DRAFT

## 7 Results

In this section, the results of the statistical combination of the 2016 diboson searches are reported.

### 7.1 Model-independent diboson resonances

The results of the combination are reported as a function of the final state, without making any assumption on the cross section and branching fractions of the heavy resonances. However, minor dependences on the simulated resonance spin are still present. Table 12 shows which analysis contribute to a particular final state.

Table 12: Contribution of each single analysis and final state to the model-independent limits.

WW	B2G-17-001	B2G-16-029		
WZ	B2G-17-001	B2G-16-029	B2G-17-005	B2G-17-013
ZZ	B2G-17-001	B2G-17-005	B2G-17-013	B2G-16-023
WH	B2G-17-002	B2G-17-004	B2G-17-006	
ZH	B2G-17-002	B2G-17-004	B2G-17-006	
HH	B2G-16-026 B2G-17-019	B2G-17-006		

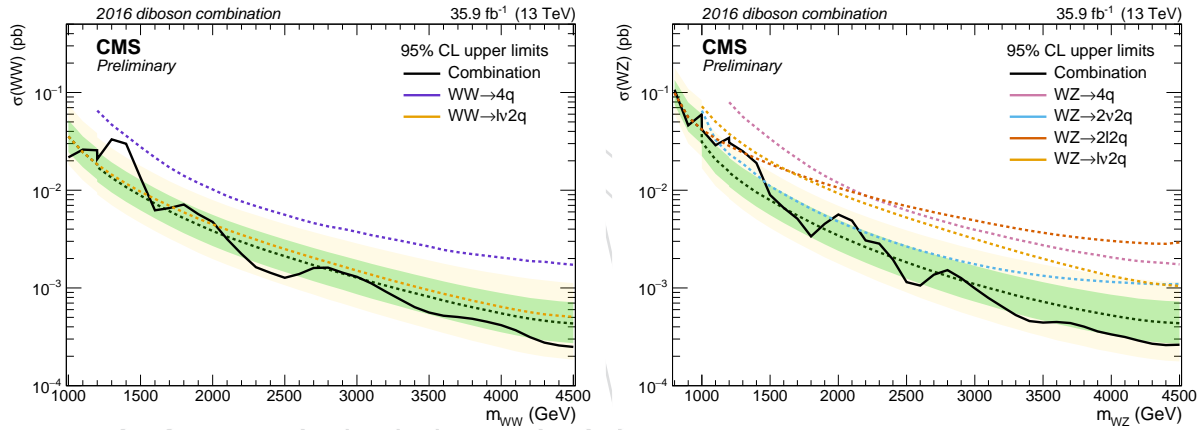


Figure 14: Combination of the diboson searches sensitive to the resonant WW (left) and WZ (right) final states. The signal acceptance has been evaluated for a spin-1 resonance.



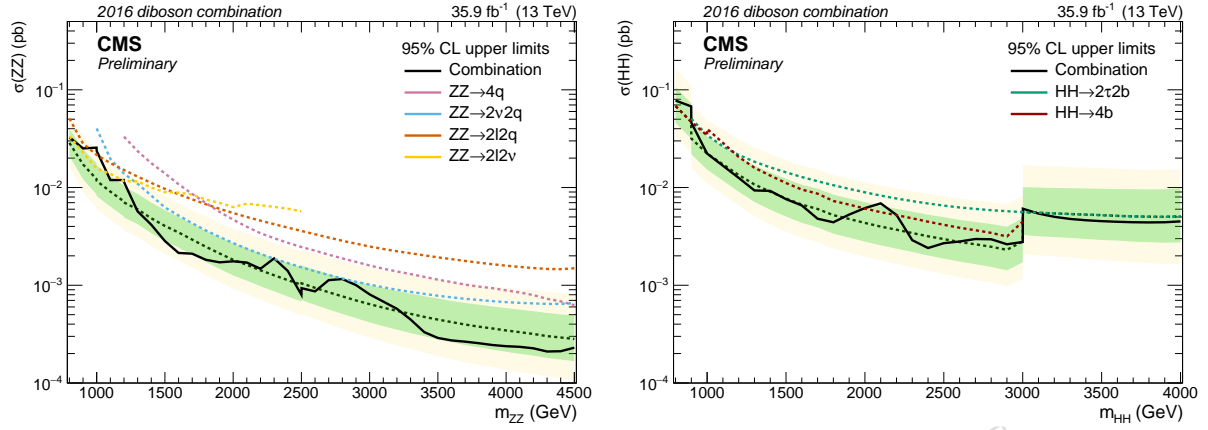


Figure 15: Combination of the diboson searches sensitive to the resonant ZZ (left) and HH (right) final states. The signal acceptance has been evaluated for a spin-1 resonance in case of the ZZ final state, and a spin-2 resonance for the HH final state.

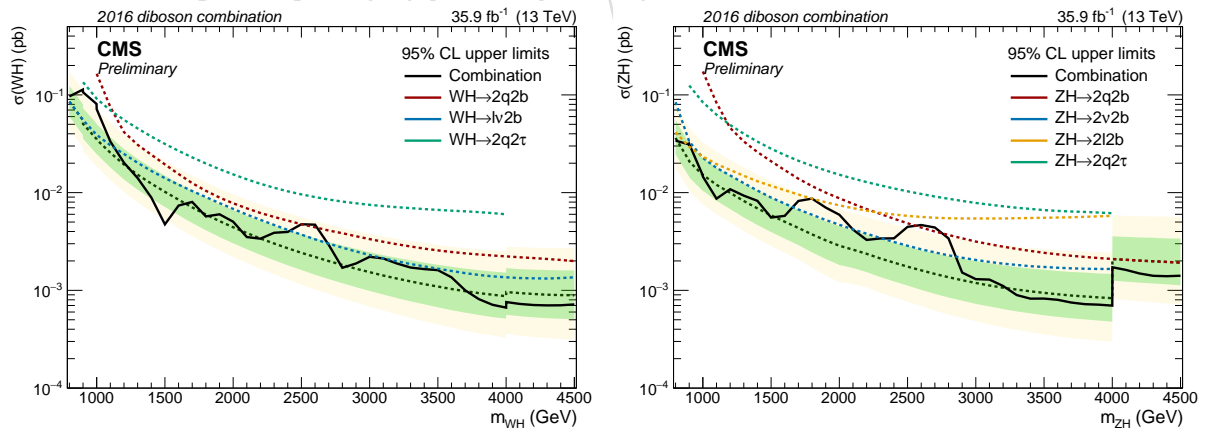


Figure 16: Combination of the diboson searches sensitive to the resonant WH (left) and ZH (right) final states. The signal acceptance has been evaluated for a spin-1 resonance.

## 7.2 $W'$ singlet hypothesis

In the  $W'$  singlet hypothesis, the  $W'$  decays to  $WZ$  and  $WH$ . All diboson analyses, except B2G-16-023 and B2G-16-026, have channels sensitive to these decays. The results in the HVT benchmark scenarios A and B are shown in Fig. 17 and 19. The EXO-16-033 analysis is included in Fig. 18.

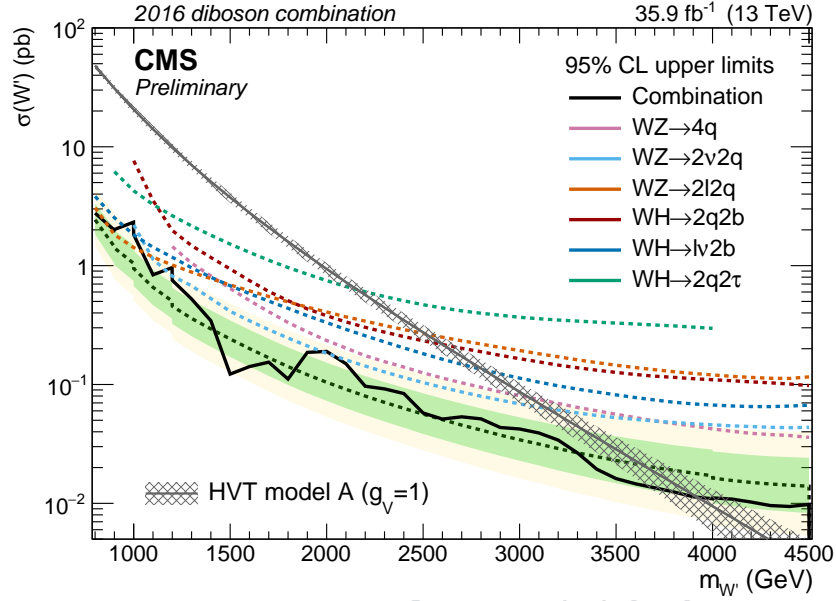


Figure 17: Exclusion limit for a narrow spin-1  $W'$  resonance in a strongly coupled scenario (HVT model A,  $g_V = 1$ ).

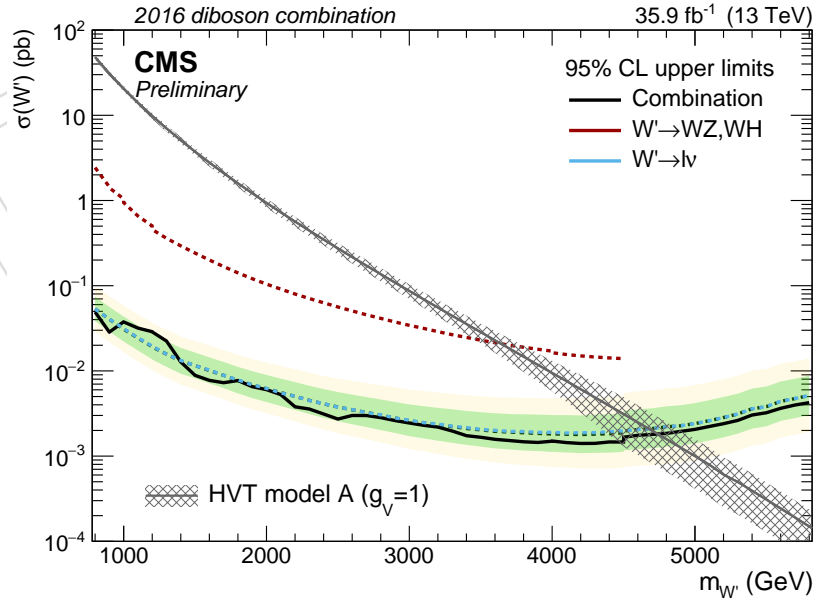


Figure 18: Exclusion limit for a narrow spin-1  $W'$  resonance in a strongly coupled scenario (HVT model A,  $g_V = 1$ ). The  $W' \rightarrow l\nu$  channel has been added to the combination.

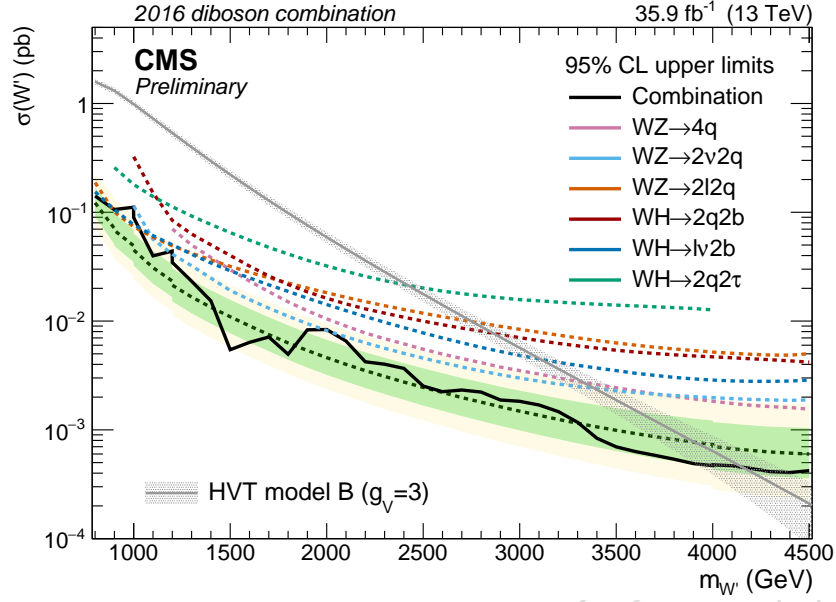


Figure 19: Exclusion limit for a narrow spin-1  $W'$  resonance in a weakly coupled scenario (HVT model B,  $g_V = 3$ ).

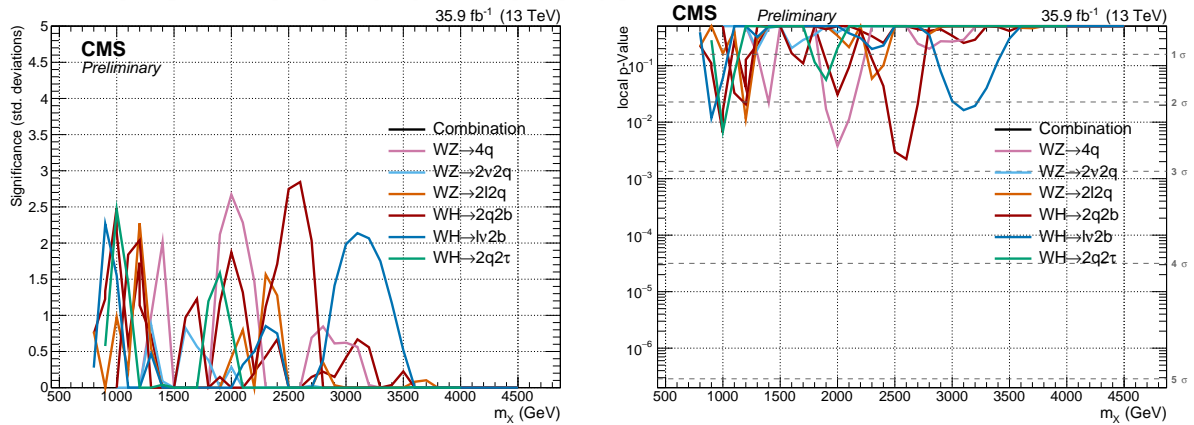


Figure 20: Significance of the excess (left) and background p-value (right) for a narrow spin-1  $W'$  resonance in a weakly coupled scenario (HVT model B,  $g_V = 3$ ).

### 7.3 $Z'$ singlet hypothesis

In the  $Z'$  singlet hypothesis, the  $Z'$  decays to  $WW$ , and  $ZH$ . All analyses, except B2G-16-023, B2G-16-026, B2G-17-005, and B2G-17-013, have channels sensitive to these decays. The results in the HVT benchmark scenarios A and B are shown in Fig. 21 and 23. The EXO-16-047 analysis is included in Fig. 22.

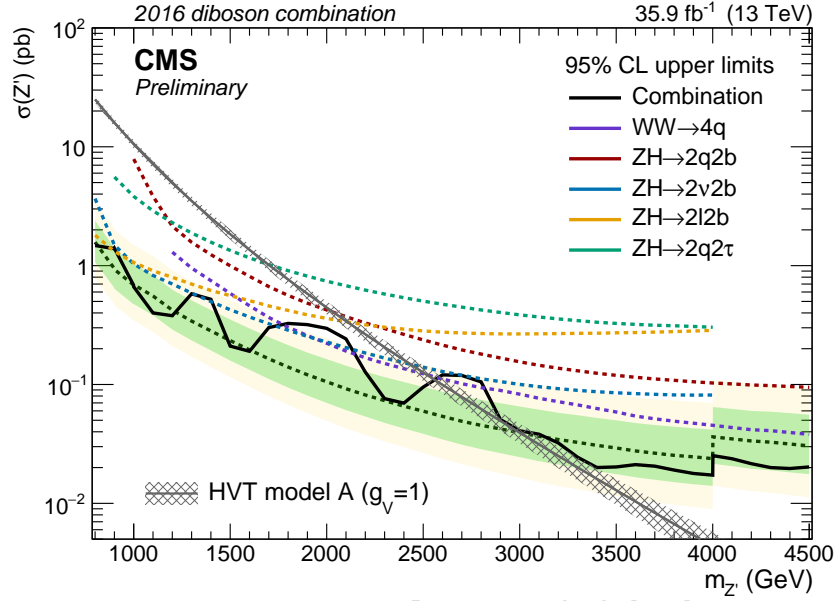


Figure 21: Exclusion limit for a narrow spin-1  $Z'$  resonance in a strongly coupled scenario (HVT model A,  $g_V = 1$ ).

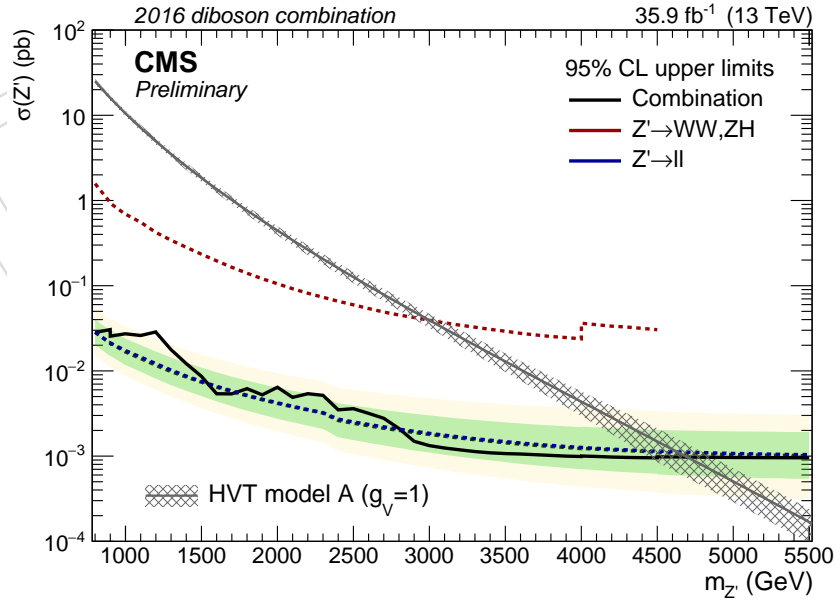


Figure 22: Exclusion limit for a narrow spin-1  $Z'$  resonance in a strongly coupled scenario (HVT model A,  $g_V = 1$ ). The  $Z' \rightarrow \ell\ell$  channel has been added to the combination.

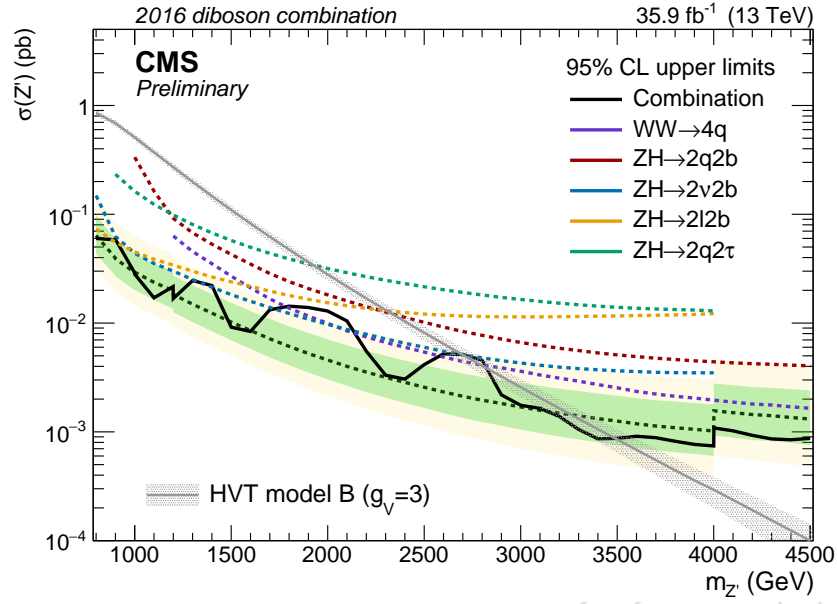


Figure 23: Exclusion limit for a narrow spin-1  $Z'$  resonance in a weakly coupled scenario (HVT model B,  $g_V = 3$ ).

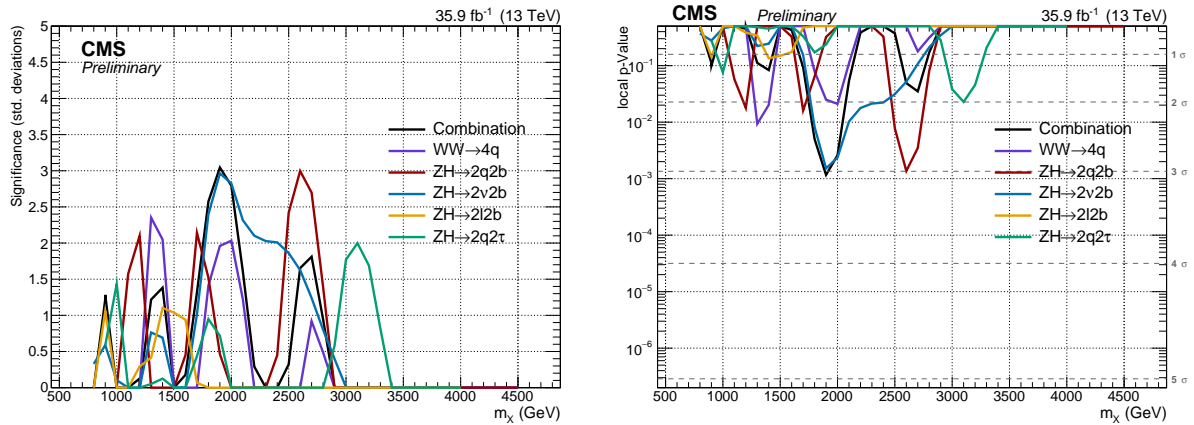


Figure 24: Significance of the excess (left) and background p-value (right) for a narrow spin-1  $Z'$  resonance in a weakly coupled scenario (HVT model B,  $g_V = 3$ ).

## 7.4 $V'$ triplet hypothesis (HVT)

In the HVT model, a mass degenerate heavy vector triplet is present, which entails that the  $W'$  and  $Z'$  have the same mass and coexist, although their cross sections are different as they are determined by the proton PDFs. All analyses, except B2G-16-023 and B2G-16-026, have channels sensitive to the decays of the  $W'$  and  $Z'$ . The results in the HVT benchmark scenarios A and B are shown in Fig. 25 and 27. The EXO-16-033 and EXO-16-047 analyses are included in Fig. 26.

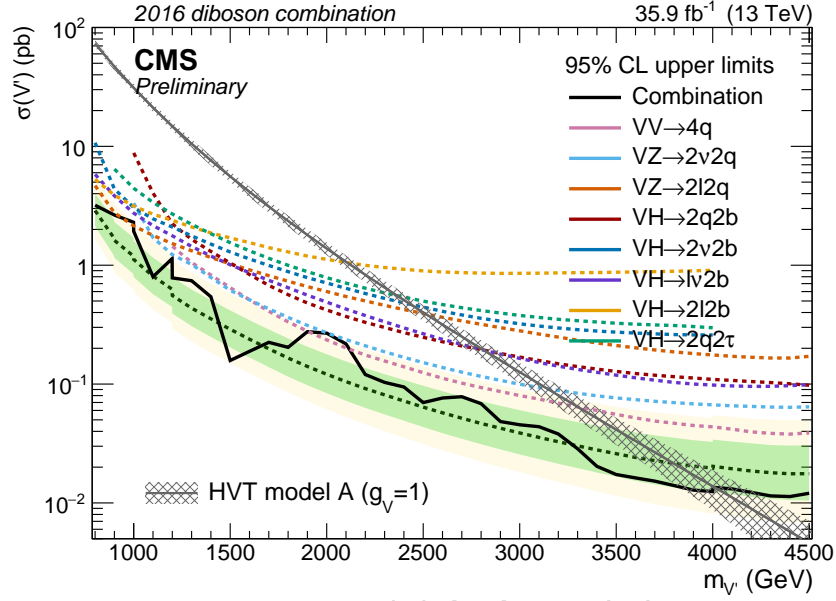


Figure 25: Exclusion limit for a narrow spin-1  $V'$  resonance in a strongly coupled scenario (HVT model A,  $g_V = 1$ ).

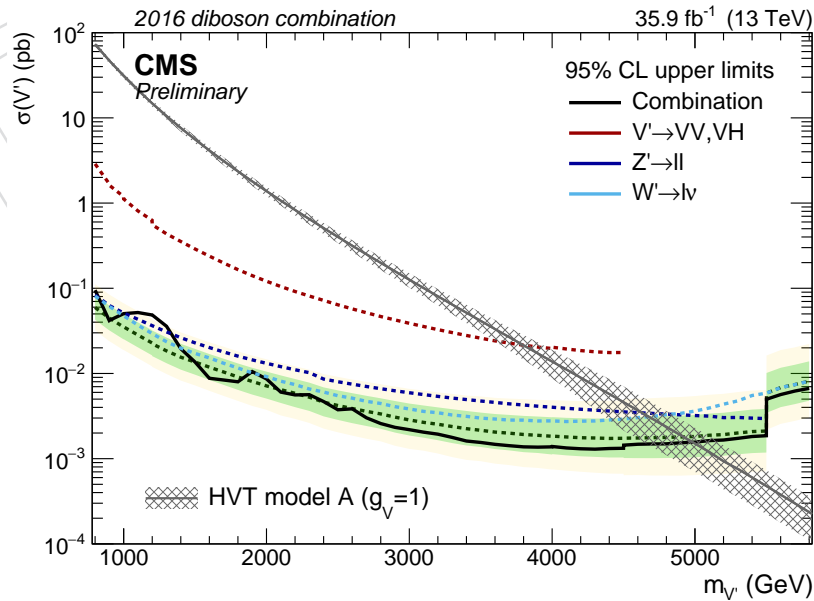


Figure 26: Exclusion limit for a narrow spin-1  $V'$  resonance in a strongly coupled scenario (HVT model A,  $g_V = 1$ ). The  $W' \rightarrow l\nu$  and  $Z' \rightarrow ll$  channel has been added to the combination.

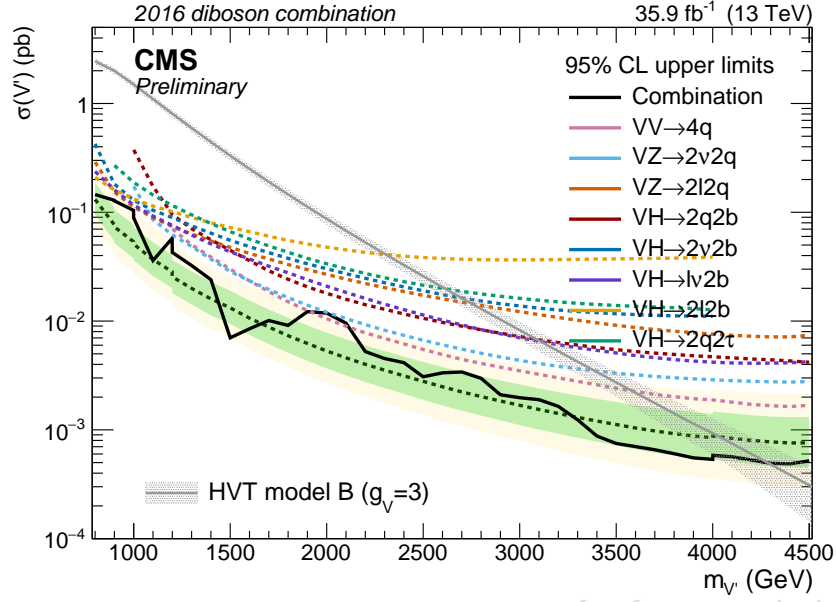


Figure 27: Exclusion limit for a narrow spin-1  $V'$  resonance in a weakly coupled scenario (HVT model B,  $g_V = 3$ ).

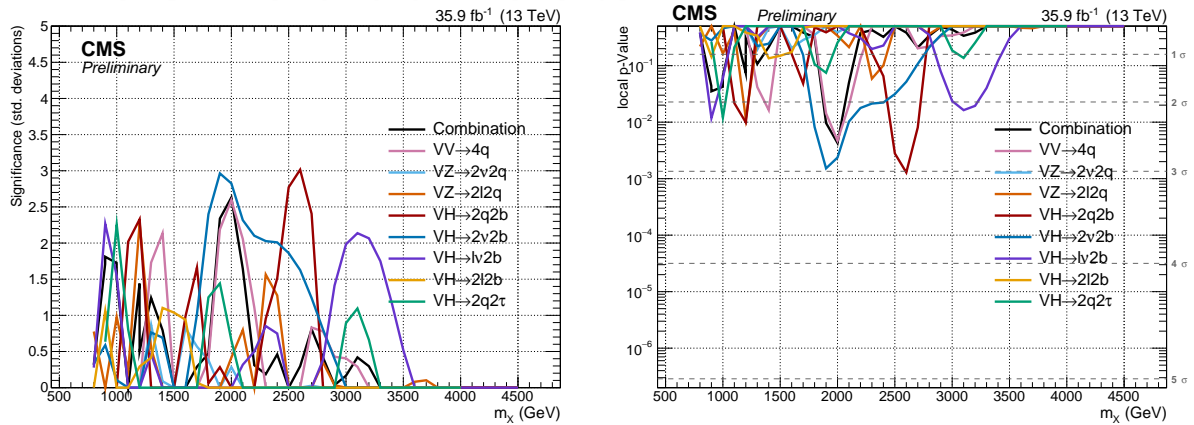


Figure 28: Significance of the excess (left) and background p-value (right) for a narrow spin-1  $V'$  resonance in a weakly coupled scenario (HVT model B,  $g_V = 3$ ).

## 7.5 Bulk Graviton

In the Bulk Graviton model, there is only a single massive resonance which decays in pairs of bosons (WW, ZZ, and HH). All analyses, except B2G-17-002 and B2G-17-004, have channels sensitive to the decays of the Bulk Graviton. The results are shown in Fig. 29.

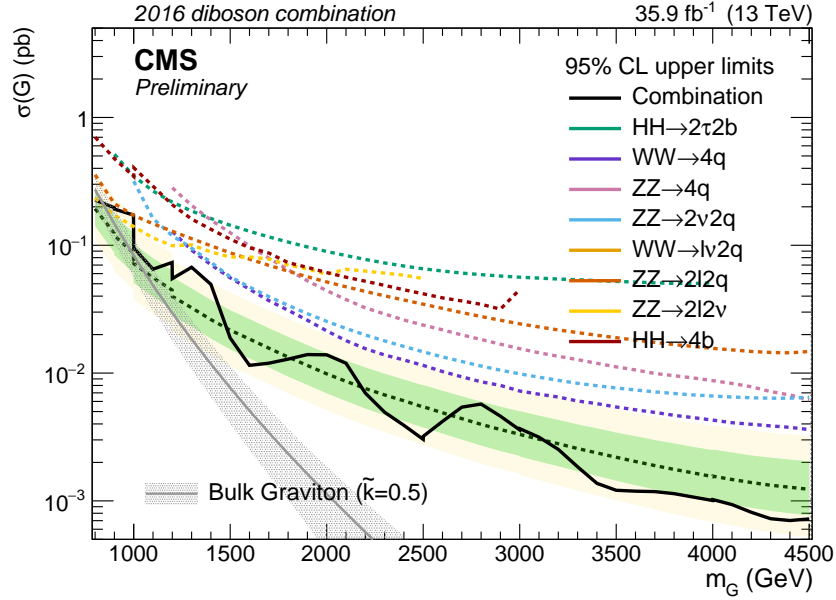


Figure 29: Exclusion limit for a narrow spin-2 Bulk Graviton.

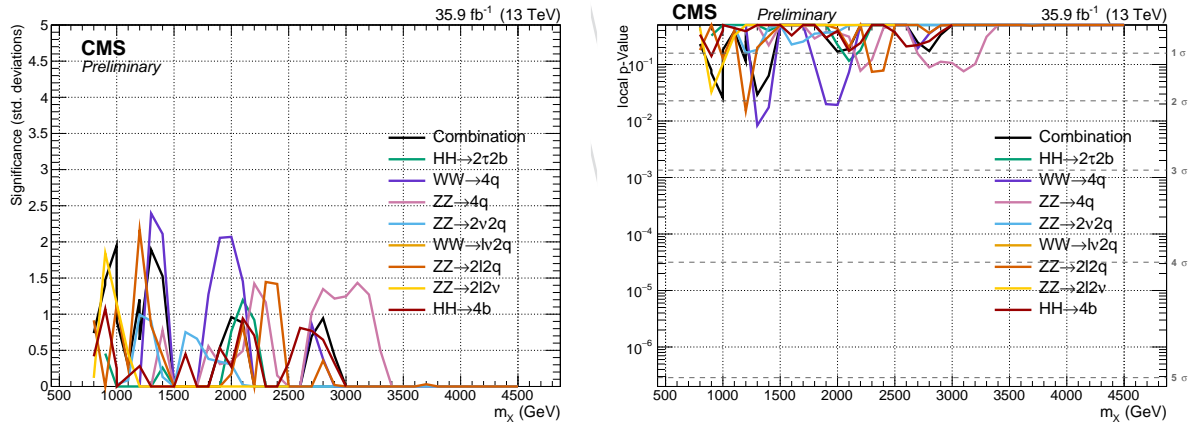


Figure 30: Significance of the excess (left) and background p-value (right) for a narrow spin-2 Bulk Graviton.



## 8 Summary

Searches for a heavy resonances with mass between 800 and 4500 GeV, decaying into a pair of vector bosons, a vector boson and a Higgs boson, or two Higgs bosons, have been performed on data collected by the CMS experiment at  $\sqrt{s} = 13$  TeV during 2016, and corresponds to integrated luminosity of  $35.9 \text{ fb}^{-1}$ . This Analysis Note describes the statistical combination of these analysis, focusing on the treatment of the systematic uncertainties across the different channels. In a triplet of narrow spin-1 resonances, heavy vectors with mass lower than 4.1 and 4.3 TeV are excluded in the benchmark scenario A and B, respectively. These results represent the most stringent limits on these models provided by CMS. By including the dominant decay modes to leptons, the masses lower than 5.0 TeV are excluded in the benchmark scenario A.

DRAFT

## References

- [1] CMS Collaboration, “Combination of searches for heavy resonances decaying to WW, WZ, ZZ, WH, and ZH boson pairs in proton-proton collisions at  $\sqrt{s} = 8$  and 13 TeV”, *Phys. Lett. B* **774** (2017) 533–558, doi:10.1016/j.physletb.2017.09.083, arXiv:1705.09171.
- [2] CMS Collaboration, “Search for ZZ resonances in the  $2\ell 2\nu$  final state in proton-proton collisions at 13 TeV”, *JHEP* **03** (2018) 003, doi:10.1007/JHEP03(2018)003, arXiv:1711.04370.
- [3] CMS Collaboration, “Search for a massive resonance decaying to a pair of Higgs bosons in the four b quark final state in proton-proton collisions at  $\sqrt{s} = 13$  TeV”, *Phys. Lett. B* **781** (2018) 244–269, doi:10.1016/j.physletb.2018.03.084, arXiv:1710.04960.
- [4] CMS Collaboration, “Search for a heavy resonance decaying to a pair of vector bosons in the lepton plus merged jet final state at  $\sqrt{s} = 13$  TeV”, *JHEP* **05** (2018) 088, doi:10.1007/JHEP05(2018)088, arXiv:1802.09407.
- [5] CMS Collaboration, “Search for massive resonances decaying into WW, WZ, ZZ,  $qW$ , and  $qZ$  with dijet final states at  $\sqrt{s} = 13$  TeV”, *Phys. Rev. D* **97** (2018), no. 7, 072006, doi:10.1103/PhysRevD.97.072006, arXiv:1708.05379.
- [6] CMS Collaboration, “Search for heavy resonances that decay into a vector boson and a Higgs boson in hadronic final states at  $\sqrt{s} = 13$  TeV”, *Eur. Phys. J. C* **77** (2017) 636, doi:10.1140/epjc/s10052-017-5192-z, arXiv:1707.01303.
- [7] CMS Collaboration, “Search for heavy resonances decaying into a vector boson and a Higgs boson in final states with charged leptons, neutrinos and b quarks at  $\sqrt{s} = 13$  TeV”, arXiv:1807.02826.
- [8] CMS Collaboration, “Search for a heavy resonance decaying into a Z boson and a vector boson in the  $\nu\bar{\nu}q\bar{q}$  final state”, *JHEP* **07** (2018) 075, doi:10.1007/JHEP07(2018)075, arXiv:1803.03838.
- [9] CMS Collaboration, “Search for heavy resonances decaying into two Higgs bosons or into a Higgs and a vector boson in proton-proton collisions at 13 TeV”,.
- [10] CMS Collaboration, “Search for a new heavy resonance decaying into a Z boson and a Z or W boson in  $2\ell 2q$  final states at  $\sqrt{s} = 13$  TeV”, arXiv:1803.10093.
- [11] CMS Collaboration, “Search for resonant and non-resonant production of Higgs boson pairs in the four b quark final state using boosted jets in proton-proton collisions at  $\sqrt{s}=13$  TeV”,.
- [12] CMS Collaboration, “Search for high-mass resonances in final states with a lepton and missing transverse momentum at  $\sqrt{s} = 13$  TeV”, *JHEP* **06** (2018) 128, doi:10.1007/JHEP06(2018)128, arXiv:1803.11133.
- [13] CMS Collaboration, “Search for high-mass resonances in dilepton final states in proton-proton collisions at  $\sqrt{s} = 13$  TeV”, *JHEP* **06** (2018) 120, doi:10.1007/JHEP06(2018)120, arXiv:1803.06292.

- [14] ATLAS and CMS Collaboration, “Combined measurement of the Higgs boson mass in  $pp$  collisions at  $\sqrt{s} = 7$  and 8 TeV with the ATLAS and CMS experiments”, *Phys. Rev. Lett.* **114** (2015) 191803, doi:10.1103/PhysRevLett.114.191803, arXiv:1503.07589.
- [15] ATLAS and CMS Collaboration, “Measurements of the Higgs boson production and decay rates and constraints on its couplings from a combined ATLAS and CMS analysis of the LHC  $pp$  collision data at  $\sqrt{s} = 7$  and 8 TeV”, *JHEP* **08** (2016) 045, doi:10.1007/JHEP08(2016)045, arXiv:1606.02266.
- [16] ATLAS Collaboration, “Observation of a new particle in the search for the standard model Higgs boson with the ATLAS detector at the LHC”, *Phys. Lett. B* **716** (2012) 1, doi:10.1016/j.physletb.2012.08.020, arXiv:1207.7214.
- [17] CMS Collaboration, “Observation of a new boson at a mass of 125 GeV with the CMS experiment at the LHC”, *Phys. Lett. B* **716** (2012) 30, doi:10.1016/j.physletb.2012.08.021, arXiv:1207.7235.
- [18] CMS Collaboration, “Observation of a new boson with mass near 125 GeV in  $pp$  collisions at  $\sqrt{s} = 7$  and 8 TeV”, *JHEP* **06** (2013) 081, doi:10.1007/JHEP06(2013)081, arXiv:1303.4571.
- [19] CMS Collaboration, “Precise determination of the mass of the Higgs boson and tests of compatibility of its couplings with the standard model predictions using proton collisions at 7 and 8 TeV”, *Eur. Phys. J. C* **75** (2015) 212, doi:10.1140/epjc/s10052-015-3351-7, arXiv:1412.8662.
- [20] ATLAS Collaboration, “Measurement of the Higgs boson mass from the  $H \rightarrow \gamma\gamma$  and  $H \rightarrow ZZ^* \rightarrow 4\ell$  channels in  $pp$  collisions at center-of-mass energies of 7 and 8 TeV with the ATLAS detector”, *Phys. Rev. D* **90** (2014) 052004, doi:10.1103/PhysRevD.90.052004, arXiv:1406.3827.
- [21] ATLAS Collaboration, “Evidence for the spin-0 nature of the Higgs boson using ATLAS data”, *Phys. Lett. B* **726** (2013) 120, doi:10.1016/j.physletb.2013.08.026, arXiv:1307.1432.
- [22] A. Belyaev et al., “Technicolor Walks at the LHC”, *Phys. Rev.* **D79** (2009) 035006, doi:10.1103/PhysRevD.79.035006, arXiv:0809.0793.
- [23] F. Sannino and K. Tuominen, “Orientifold theory dynamics and symmetry breaking”, *Phys. Rev.* **D71** (2005) 051901, doi:10.1103/PhysRevD.71.051901, arXiv:hep-ph/0405209.
- [24] R. Foadi, M. T. Frandsen, T. A. Rytlov, and F. Sannino, “Minimal Walking Technicolor: Set Up for Collider Physics”, *Phys. Rev.* **D76** (2007) 055005, doi:10.1103/PhysRevD.76.055005, arXiv:0706.1696.
- [25] T. Han, H. E. Logan, B. McElrath, and L.-T. Wang, “Phenomenology of the little Higgs model”, *Phys. Rev. D* **67** (2003) 095004, doi:10.1103/PhysRevD.67.095004, arXiv:hep-ph/0301040.
- [26] M. Schmaltz and D. Tucker-Smith, “Little Higgs theories”, *Ann. Rev. Nucl. Part. Sci.* **55** (2005) 229, doi:10.1146/annurev.nucl.55.090704.151502, arXiv:hep-ph/0502182.

- [27] M. Perelstein, “Little Higgs models and their phenomenology”, *Prog. Part. Nucl. Phys.* **58** (2007) 247, doi:10.1016/j.pnpnp.2006.04.001, arXiv:hep-ph/0512128.
- [28] R. Contino, D. Pappadopulo, D. Marzocca, and R. Rattazzi, “On the effect of resonances in composite Higgs phenomenology”, *JHEP* **10** (2011) 081, doi:10.1007/JHEP10(2011)081, arXiv:1109.1570.
- [29] D. Marzocca, M. Serone, and J. Shu, “General composite Higgs models”, *JHEP* **08** (2012) 13, doi:10.1007/JHEP08(2012)013, arXiv:1205.0770.
- [30] B. Bellazzini, C. Csaki, and J. Serra, “Composite Higgses”, *Eur. Phys. J. C* **74** (2014) 2766, doi:10.1140/epjc/s10052-014-2766-x, arXiv:1401.2457.
- [31] D. Pappadopulo, A. Thamm, R. Torre, and A. Wulzer, “Heavy vector triplets: bridging theory and data”, *JHEP* **09** (2014) 60, doi:10.1007/JHEP09(2014)060, arXiv:1402.4431.
- [32] L. Randall and R. Sundrum, “Large mass hierarchy from a small extra dimension”, *Phys. Rev. Lett.* **83** (1999) 3370, doi:10.1103/PhysRevLett.83.3370, arXiv:hep-ph/9905221.
- [33] L. Randall and R. Sundrum, “An alternative to compactification”, *Phys. Rev. Lett.* **83** (1999) 4690, doi:10.1103/PhysRevLett.83.4690, arXiv:hep-th/9906064.
- [34] CMS Collaboration, “Performance of electron reconstruction and selection with the CMS detector in proton-proton collisions at  $\sqrt{s} = 8$  TeV”, *JINST* **10** (2015) P06005, doi:10.1088/1748-0221/10/06/P06005, arXiv:1502.02701.
- [35] CMS Collaboration, “Performance of CMS muon reconstruction in pp collision events at  $\sqrt{s} = 7$  TeV”, *JINST* **7** (2012) P10002, doi:10.1088/1748-0221/7/10/P10002, arXiv:1206.4071.
- [36] CMS Collaboration, “Tau identification in boosted topologies”, CMS Detector Performance Summary CMS-DP-2016-038, CERN, 2016.
- [37] CMS Collaboration, “Pileup removal algorithms”, CMS Physics Analysis Summary CMS-PAS-JME-14-001, CERN, 2014.
- [38] CMS Collaboration, “Jet energy scale and resolution in the CMS experiment in pp collisions at 8 TeV”, *JINST* **12** (2017) P02014, doi:10.1088/1748-0221/12/02/P02014, arXiv:1607.03663.
- [39] D. Bertolini, P. Harris, M. Low, and N. Tran, “Pileup per particle identification”, *JHEP* **10** (2014) 59, doi:10.1007/JHEP10(2014)059, arXiv:1407.6013.
- [40] M. Dasgupta, A. Fregoso, S. Marzani, and G. P. Salam, “Towards an understanding of jet substructure”, *JHEP* **09** (2013) 029, doi:10.1007/JHEP09(2013)029, arXiv:1307.0007.
- [41] A. J. Larkoski, S. Marzani, G. Soyez, and J. Thaler, “Soft drop”, *JHEP* **05** (2014) 146, doi:10.1007/JHEP05(2014)146, arXiv:1402.2657.
- [42] CMS Collaboration, “Jet algorithms performance in 13 TeV data”, CMS Physics Analysis Summary CMS-PAS-JME-16-003, CERN, 2017.

- [43] J. Thaler and K. Van Tilburg, “Identifying boosted objects with N-subjettiness”, *JHEP* **03** (2011) 015, doi:10.1007/JHEP03(2011)015, arXiv:1011.2268.
- [44] CMS Collaboration, “Identification of double-b quark jets in boosted event topologies”, CMS Physics Analysis Summary CMS-PAS-BTV-15-002, CERN, 2016.
- [45] CMS Collaboration, “Identification of b quark jets at the CMS Experiment in the LHC Run 2”, CMS Physics Analysis Summary CMS-PAS-BTV-15-001, CERN, 2016.
- [46] G. Altarelli, B. Mele, and M. Ruiz-Altaba, “Searching for new heavy vector bosons in  $p\bar{p}$  colliders”, *Z. Phys. C* **45** (1989) 109, doi:10.1007/BF01552335. [Erratum: doi:10.1007/BF01556677].
- [47] G. Cowan, K. Cranmer, E. Gross, and O. Vitells, “Asymptotic formulae for likelihood-based tests of new physics”, *Eur. Phys. J. C* **71** (2011) 1554, doi:10.1140/epjc/s10052-011-1554-0, arXiv:1007.1727. [Erratum: doi:10.1140/epjc/s10052-013-2501-z].